

AD

(Leave blank)

Award Number: W81XWH-09-1-0299

TITLE: Photoacoustic Imaging of Epilepsy

PRINCIPAL INVESTIGATOR: Huabei Jiang, PhD

CONTRACTING ORGANIZATION: University of Florida
Gainesville, FL 32611

REPORT DATE: April 2011

TYPE OF REPORT: Annual

PREPARED FOR: U.S. Army Medical Research and Materiel Command
Fort Detrick, Maryland 21702-5012

DISTRIBUTION STATEMENT:

Approved for public release; distribution unlimited

The views, opinions and/or findings contained in this report are those of the author(s) and should not be construed as an official Department of the Army position, policy or decision unless so designated by other documentation.

REPORT DOCUMENTATION PAGE

Form Approved
OMB No. 0704-0188

Public reporting burden for this collection of information is estimated to average 1 hour per response, including the time for reviewing instructions, searching existing data sources, gathering and maintaining the data needed, and completing and reviewing this collection of information. Send comments regarding this burden estimate or any other aspect of this collection of information, including suggestions for reducing this burden to Department of Defense, Washington Headquarters Services, Directorate for Information Operations and Reports (0704-0188), 1215 Jefferson Davis Highway, Suite 1204, Arlington, VA 22202-4302. Respondents should be aware that notwithstanding any other provision of law, no person shall be subject to any penalty for failing to comply with a collection of information if it does not display a currently valid OMB control number. PLEASE DO NOT RETURN YOUR FORM TO THE ABOVE ADDRESS.

1. REPORT DATE (DD-MM-YYYY) 04-30-2011	2. REPORT TYPE Annual	3. DATES COVERED (From - To) 01 APR 2010 - 31 MAR 2011	
4. TITLE AND SUBTITLE Photoacoustic Imaging of Epilepsy		5a. CONTRACT NUMBER W81XWH-09-1-0299	
		5b. GRANT NUMBER PR080678	
		5c. PROGRAM ELEMENT NUMBER	
6. AUTHOR(S) Huabei Jiang, PhD hjiang@bme.ufl.edu		5d. PROJECT NUMBER	
		5e. TASK NUMBER	
		5f. WORK UNIT NUMBER	
7. PERFORMING ORGANIZATION NAME(S) AND ADDRESS(ES) University of Florida Biomedical Sciences Building Gainesville, FL 32611		8. PERFORMING ORGANIZATION REPORT NUMBER	
9. SPONSORING / MONITORING AGENCY NAME(S) AND ADDRESS(ES) U.S. Army Medical Research and Materiel Command Fort Detrick, Maryland		10. SPONSOR/MONITOR'S ACRONYM(S)	
		11. SPONSOR/MONITOR'S REPORT NUMBER(S)	
12. DISTRIBUTION / AVAILABILITY STATEMENT Approved for public release; distribution unlimited			
13. SUPPLEMENTARY NOTES Photoacoustic imaging, photoacoustic tomography, epilepsy, seizure			
14. ABSTRACT This research is aimed at developing a new imaging approach, called "Photoacoustic tomography (PAT)", for non-invasively tracking dynamical changes during seizure occurrence. The project will develop imaging hardware and software, and conduct phantom/in vivo experiments to achieve the proposed goals. During the second year of this project, we have completed the construction of the proposed array based PAT system, and calibrated and tested the system using extensive phantom experiments. We have also built an animal interface and successfully tested it for in vivo imaging of rat brain. We have implemented three novel schemes that can enhance our current reconstruction software. We have conducted phantom experiments that confirmed our software enhancement.			
15. SUBJECT TERMS - None provided.			
16. SECURITY CLASSIFICATION OF: a. REPORT U		17. LIMITATION OF ABSTRACT UU	18. NUMBER OF PAGES 48
b. ABSTRACT U		19a. NAME OF RESPONSIBLE PERSON USAMRMC	
c. THIS PAGE U		19b. TELEPHONE NUMBER (include area code)	

Table of Contents

	<u>Page</u>
Introduction.....	1
Body.....	1
Key Research Accomplishments.....	18
Reportable Outcomes.....	18
Conclusion.....	19
References.....	
Appendices.....	20

Introduction

Approximately 2.5 million Americans live with epilepsy and epilepsy-related deficits today, more than disabled by Parkinson disease or brain tumors. The impact of epilepsy in the US is significant with a total cost to the nation for seizures and epilepsy of approximately \$12.5 billion. Epilepsy consists of more than 40 clinical syndromes affecting 40 million people worldwide. Approximately 25 percent of individuals receiving antiepileptic medication have inadequate seizure control; however, 80% individuals with medication resistant epilepsy might be cured through surgery if one were able to precisely localize the seizure focus. The proposed research will significantly advance our ability to localize such foci, and thereby offer curative epilepsy surgery for this devastating disease. Photoacoustic tomography (PAT) uniquely combines the high contrast advantage of optical imaging and the high resolution advantage of ultrasound imaging in a single modality. In addition to high resolution structural information, the proposed PAT is also able to provide functional information that are strongly correlated with regional or focal seizure activity, including blood volume and blood oxygenation because of the high sensitivity of optical contrast to oxyhemoglobin and deoxyhemoglobin concentrations. The hypothesis of the proposed research is that PAT offers the possibility to non-invasively track dynamical changes during seizure occurrence. The overall goal of this research is to advance a finite element based photoacoustic tomography method for epilepsy imaging, using both laboratory and *in vivo* experiments. Specifically, in this project we propose: (1) To design, construct and test a transducer array system for both 2D and 3D PAT imaging; (2) To advance reconstruction algorithms and associated image enhancement schemes for quantitative PAT; (3) To evaluate and optimize the integrated functioning of the hardware and software components of the transducer array-based system, using simulation and phantom experiments; (4) To test and validate the PAT system using a well established animal model of temporal lobe epilepsy.

Body

This report describes work accomplished in Year 2 (Months 12-24) of the project. As outlined in the approved Statement of Work (SOW), the tasks during this period of time include: **Task 1** (Months 0-24): Assemble the entire photoacoustic tomography (PAT) system; **Task 2** (Months 18-24): Design, build and test the animal interfaces; thus the PAT system is ready for *in vivo* studies; **Task 3** (Months 12-24): Implement reconstruction codes and associated enhancing schemes including dynamic dual meshing, initial parameter optimization and reconstruction of absolute optical absorption coefficient for quantitative high resolution functional PAT; and **Task 4** (Months 12-24): Calibrate the imaging system; conduct simulation and extensive phantom experiments using the system for evaluation of the reconstruction codes and associated enhancements.

The sections below consist of (1) system development and evaluation and (2) software development that reflect the tasks associated with the SOW during Months 12-24.

1. System Development and Evaluation (Tasks 1, 2 and 4)

We are pleased to report that we have successfully constructed, tested and calibrated the proposed transducer array based real-time PAT system in Year 2. Here we provide detailed description of this novel PAT system, and present the calibration and experimental studies using this system. Figs. 1a and 1b show the photograph of the completed PAT system.

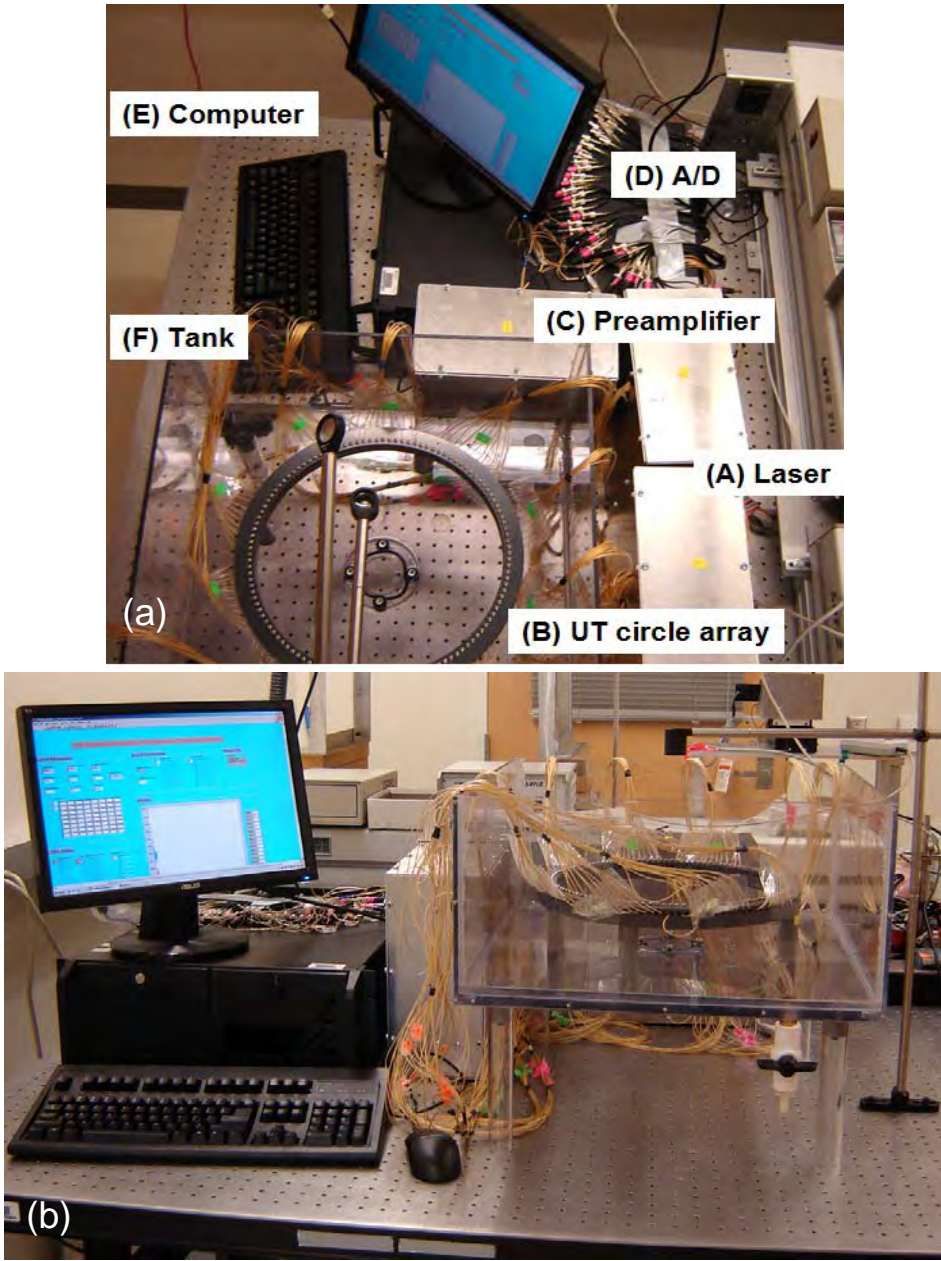


Figure 1. Photograph of the real-time PAT system. (a): Top view. (b): Front view.

As shown in Fig. 1a, a tunable Ti:Sapphire laser (part A) is used to provide 690-950nm near-infrared (NIR) laser pulses with a full-width half-maximum (FWHM) value of 8-25ns pulse width with a repetition rate of 10Hz for generating photoacoustic signals. The 5 MHz full-ring transducer array (part B) is used for recording the photoacoustic signals. A home made preamplifier (part C) receives the signals from the transducers and transmitted the amplified signals to A/D board (part D) which are then stored in the computer (part E). The three key components of the system including the tunable laser, ultrasound transducer array and acquisition system are discussed in detail in Sections 1.1-1.3 below.

Figure 2 depicts the system block diagram which allows better understanding of the data acquisition flow in this PAT system. The Ti:Sapphire laser optically pumped by a Q-switched Nd:YAG laser delivers 8 to 25-ns pulses at 10 Hz with a wavelength tunable from 690 to 950 nm

to generate photoacoustic signals. The 192-element transducer array is used to capture the photoacoustic signals. In the full 192-element configuration, 16 preamplifier boards, each supporting 12 channels, amplify the signals from the transducer elements with programmable gains of 26 dB. The multiplexed signal is subsequently amplified with an AD604 amplifier with programmable gain of 0 to 80 dB, and then digitized with the 8x8 channels A/D board. The timing for data acquisition is specifically shown in Figure 3. We see that the timer/controller contains a 10 Hz laser Q-switch signal repeated each 100ms (the Q-switch pulse width is 100us, and laser pulse width is 10ns). Three scan enabling signals, 'EN_CH1-64', 'EN_CH65-128' and 'EN_CH129-192' are synchronized by the Q-switch signal with a 3.33Hz frequency (period 300ms). EN_CH1-64 enables the #1~#64 channels pre-amplifier and data acquisition. Each channel has a sample rate of 50MHz, controlled by signal 'CLK50M' (frequency variable). The post delay and the sample waveform length are variable and can be assigned by Labview program. EN_CH65-128 enables the #65~#128 channels pre-amplifier and data acquisitions. EN_CH129-192 enables the #129~#192 channels pre-amplifier and data acquisitions. This provides the opportunity to read all captured pointers into the computer through the local bus after the acquisition and later easy readout of the photoacoustic data from all channels.

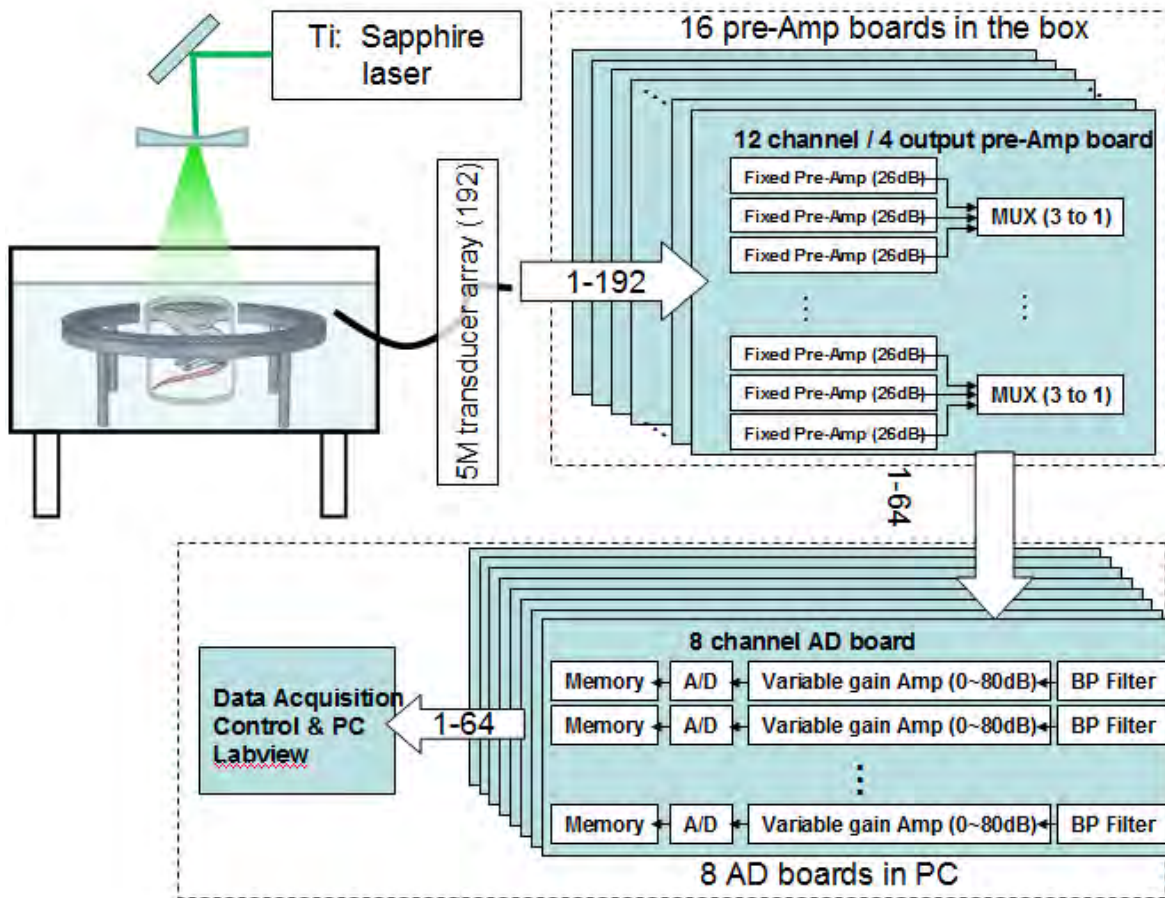


Figure 2. Block diagram of the real-time PAT system.

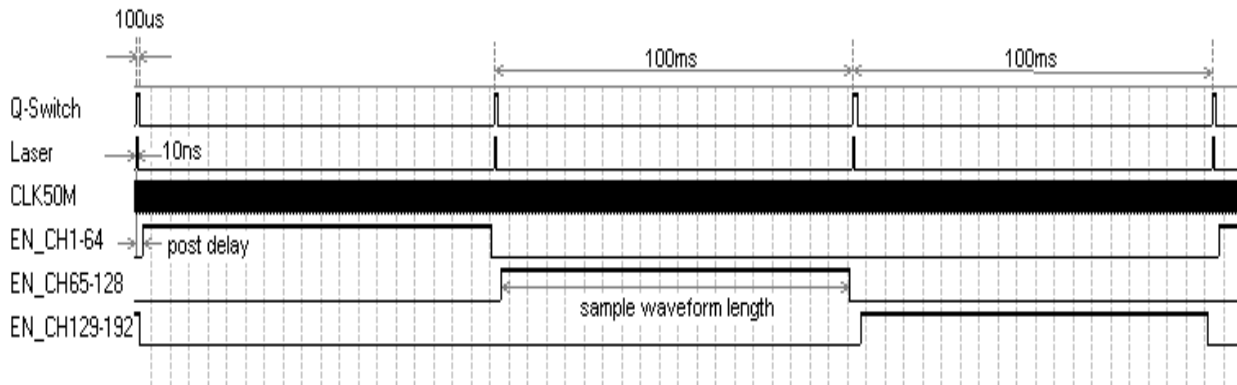


Figure 3 Diagram of timing in the PAT system.

1.1 Laser Source

A Ti:Sapphire (Symphotonics TII, LT-2211A) laser optically pumped with a Q-switched Nd:YAG laser (Symphotonics-TII, LS-2137/2) delivers 8-30 ns pulses at 10 Hz with wavelength tunable from 690 to 1000 nm. The beam is expanded with a Galilean telescope assembly and subsequently diverged with either a plano-concave lens or homogenized by a circular profile engineered diffuser (ED1-S20, ThorLabs, Newton, NJ). The laser beam is positioned at the center of the transducer and strikes the stage orthogonal to the imaging plane of the transducer for maximum uniformity.

1.2 Full-ring Ultrasound Transducer Array

Based on the extensive simulation and phantom experiments in Year 1, we eventually built the transducer array, custom manufactured by Blatek, Inc. (PA, USA), consists of 192 elements arranged in a full circular path (360 degrees) with a radius of 150 mm (Figure 4). The transducer array has a central frequency of 5 MHz and a bandwidth greater than 75%. Each element is spaced with a lateral pitch of 8 mm and has an active area of 3 mm diameter.

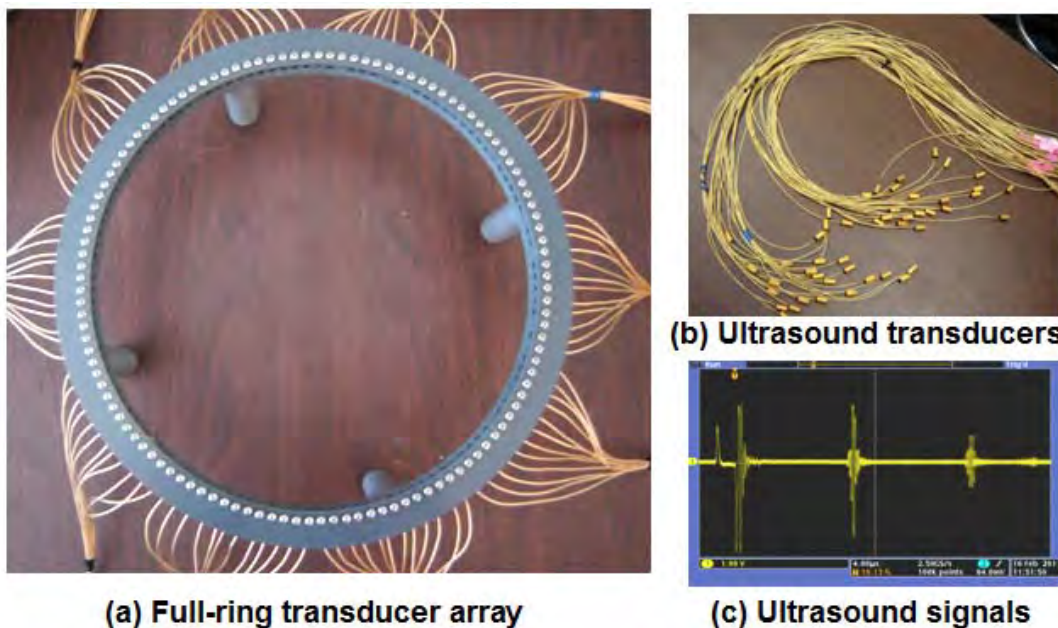


Figure 4 Full-ring ultrasound transducer array.

1.3 Control Electronics and Data Acquisition

The 192 channels photoacoustic data acquisition system is composed of 4 pre-amplifier/multiplexer boxes and 8 PCIAD850 data acquisition boards (Figure 5). Each pre-amplifier/multiplexer box includes 4 boards with 4x12 AD8099 chips and 4x4 MAX4051 chips. The whole system has 192 AD8099 (26dB) and 64 MAX4051 chips. Each PCIAD850 has 8 channels with a sample clock up to 50MHz and 10bit A/D converter. The system can sample 64 channels at one time. The #1 PCIAD850 synchronizes with the laser Q-switch sync-signal. The computer sends out the scan enabling signals by the USB-1024ls.

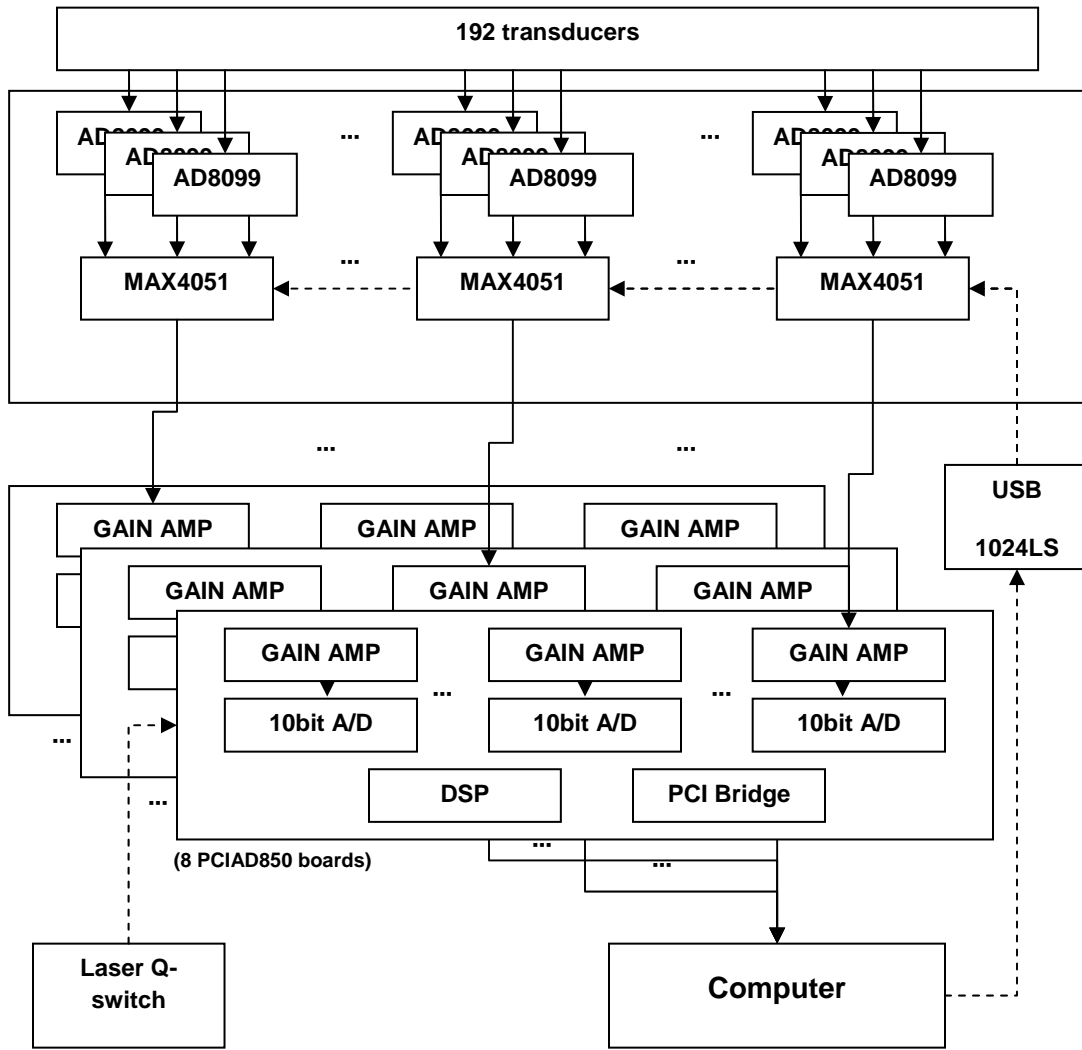


Figure 5 Flow diagram of the 192 channels photoacoustic data acquisition system.

1.3.1 The first order 26dB pre-amplifier

In the first order 26dB pre-amplifier, the AD8099 was choose to amplify the signal (Fig. 6a). In the circuit path, R1 should be 50ohm, Rf 499ohm, Rg 26ohm (Fig. 6b).

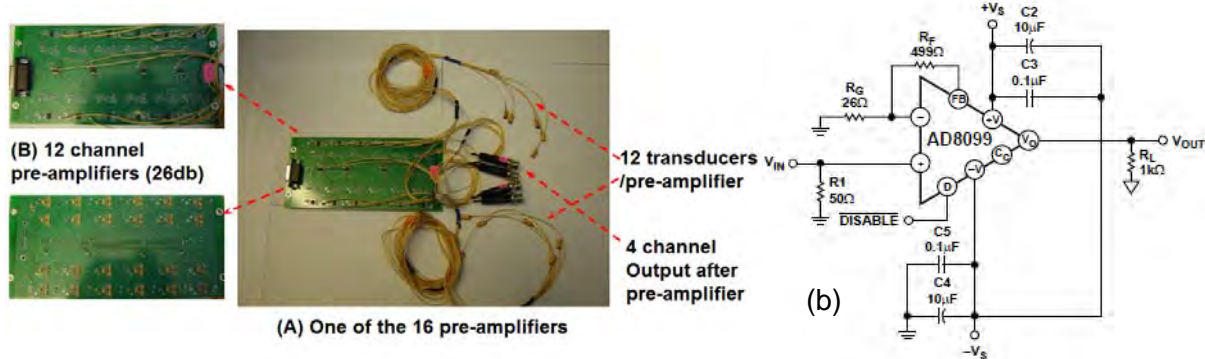


Figure 6. (a) Photograph of the 26dB pre-amplifier. (b) 26dB AD8099 design.

1.3.2 The second order 26dB pre-amplifier and 52dB pre-amplifier

As a backup plan in case of an ultra-low input signal, a 52dB gain preamplifier has been designed (Figure 7).

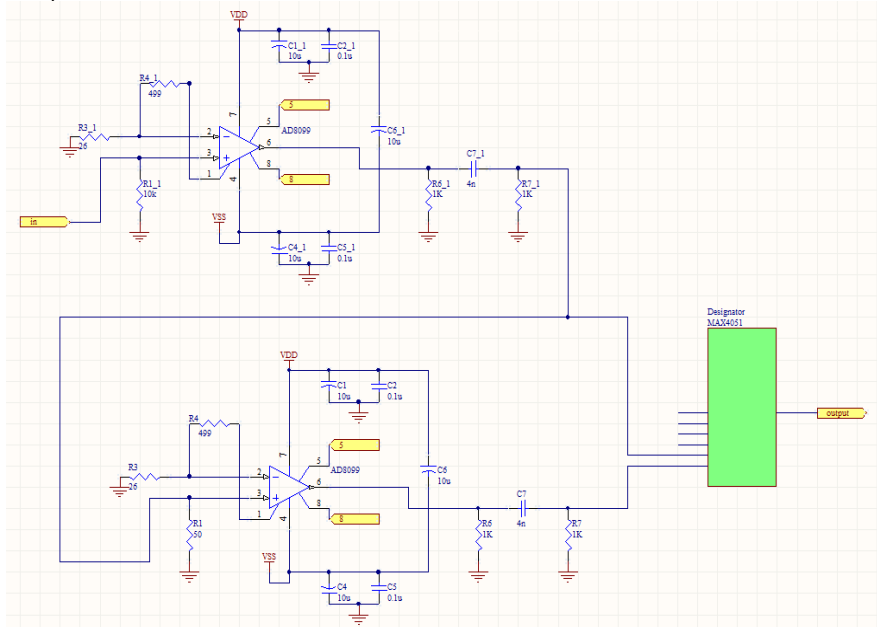


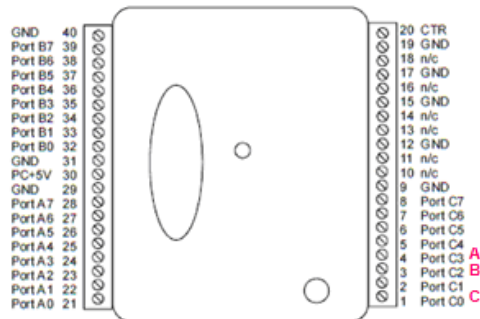
Figure 7. 26dB and 52dB AD8099 design.

1.3.3 Multiplexer MAX4051

The MAX4051 is used as a 3 to1 switch having a ± 5 V DC power supply (Figure 8A-E). The addition of diodes (Figure 9E) reduces the analog signal range to one diode drop below V+ and one diode drop above V-, without affecting the device's low switch resistance and low leakage characteristics. Here the difference between V+ and V- should not exceed 17V.



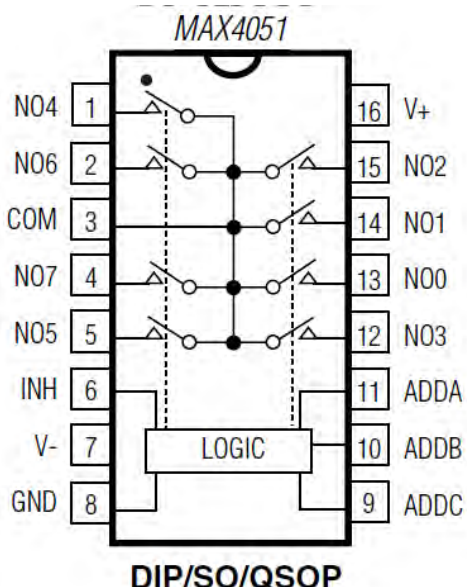
(A) USB-1024LS



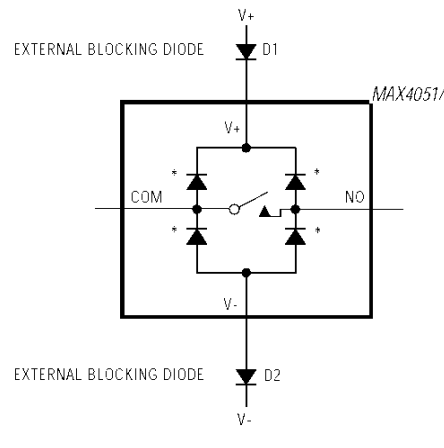
(B) Main connector and pin out

Channel	ADDA	ADDDB
9_26dB	0	0
5_26dB	0	1
1-26dB	1	0
10_26dB	0	0
6_26dB	0	1
2_26dB	1	0
11_26dB	0	0
7_26dB	0	1
3_26dB	1	0
12_26dB	0	0
8_26dB	0	1
4_26dB	1	0

(C) Truth Tabel for MUX



(D) MAX4051



* INTERNAL PROTECTION DIODES

(E) External protect diode.

Figure 8 Design of the MAX4051 as a 3 to1 switch.

1.3.4 The pre-amplifier/multiplexer board

The whole system has 4 pre-amplifier and multiplexer boxes; each box has 4 pre-amplifier and multiplexer boards. On each board, there are 12 analog input channels and 4 multiplexers providing 4 amplified outputs (Figure 9). Each analog input channel can have a gain of 26dB or 52dB.

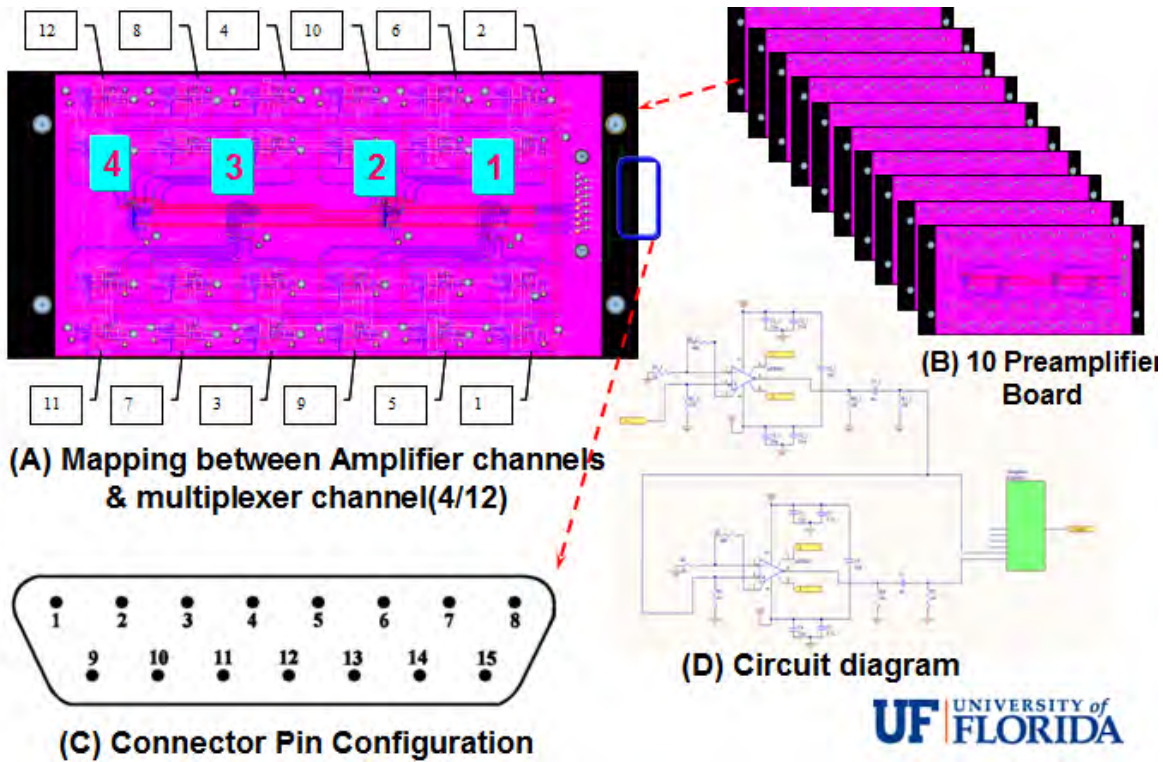


Figure 9. Schematic of the pre-amplifier and multiplexer PCB board.

1.3.5 PCIAD850

PCIAD850 is an analog-to-digital data converter (two boards) with simultaneous acquisition ability. Each PCIAD850 supports 8 channels, see Figure 10. At each trigger event (software trigger or external trigger), all the channels will simultaneously convert the analog signals to digital data with user selected post trigger delay and waveform length. Other programmable parameters include sampling rate, trigger source, trigger rate, gain, DC offset, low and high pass filters. Both boards feature user-selectable 10-bit resolution and up to 50 megabyte samples per second. With one board set as the master and remaining set to slave mode, all channels on the slave boards will start taking data upon receiving a trigger signal from the master board. The jitter between channels is less than 2 nanoseconds. PCIAD850 has low pass filters with different cutoff frequency: All frequency, 16 MHz, 7.3 MHz, and 4.8 MHz. It also has high pass filters with different cutoff frequency: 4.8 MHz, 1.6 MHz, 0.6 MHz, and 0.016 MHz. The channel based parameters:

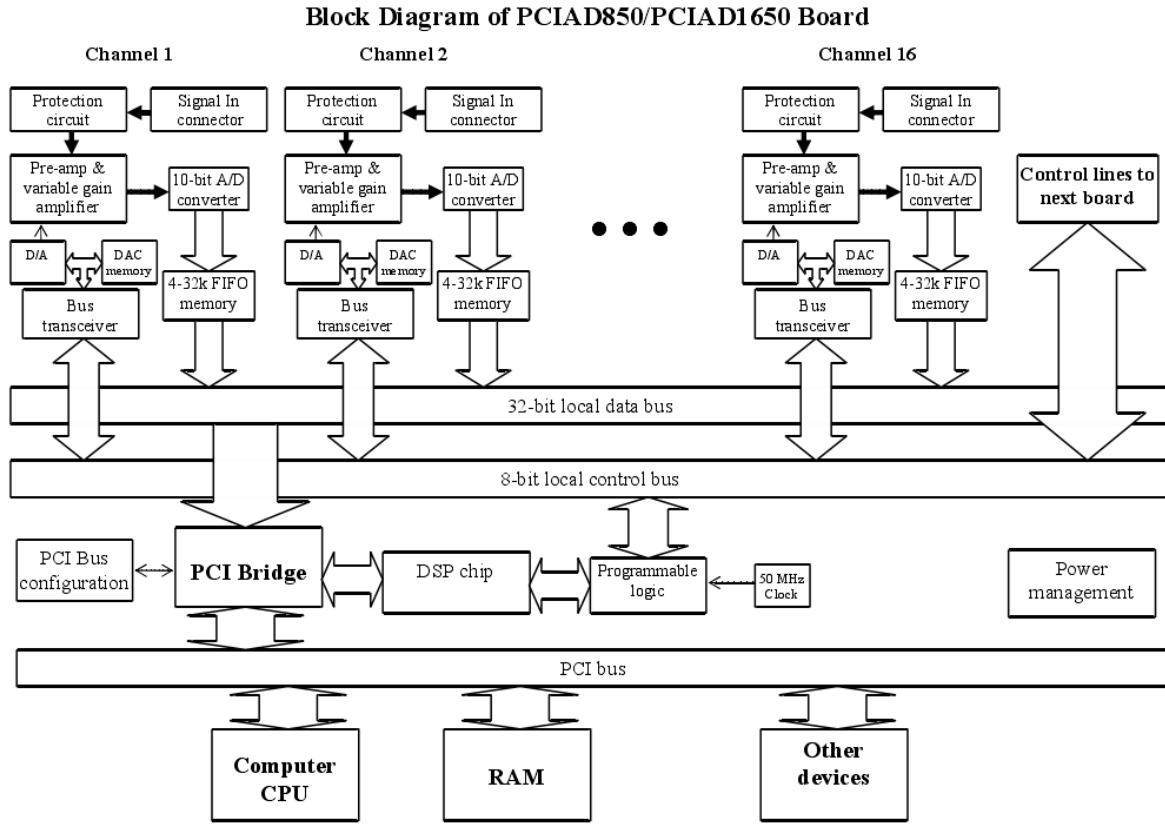


Figure 10. Block diagram of PCIAD850/1650

1.3.6 Labview Data Acquisition Software

Labview programming is used to control the entire data acquisition. The software is written to allow maximum flexibility for various system configurations. Pointers created during the data acquisition process are used to quickly access the photoacoustic data. Data is then saved for image reconstructions. Figure 11 shows the front control panel of the Labview software.

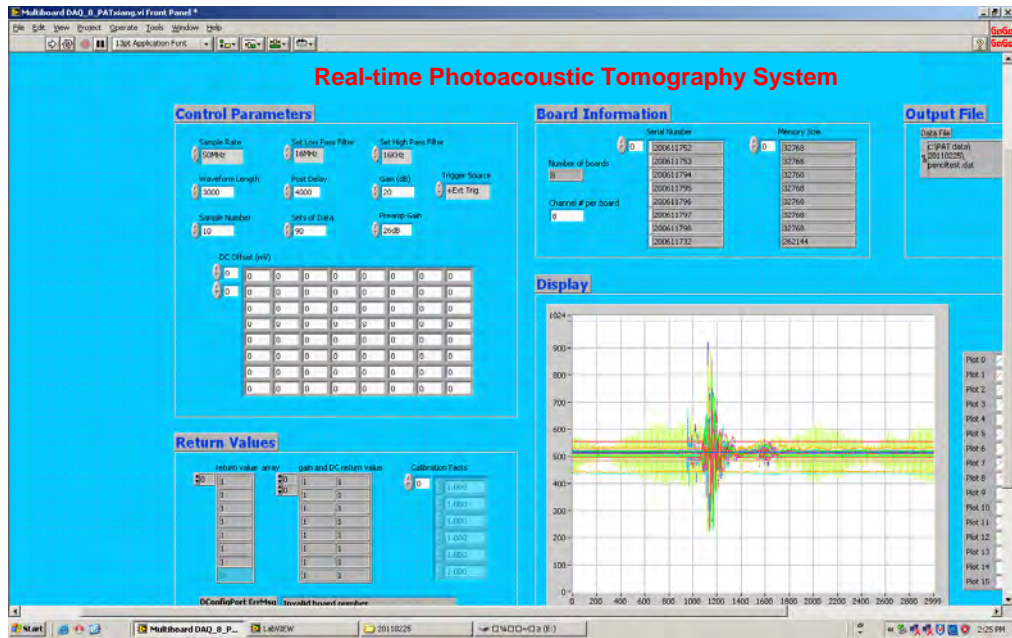


Figure 11. Front control panel of the Labview software.

1.4 System Evaluation and Experimental Studies

1.4.1 System Calibration

The system calibration is primarily concerned with the calibration of the positioning and response of the multiple transducers in the system. We used a photoacoustic (PA) point target centrally located to achieve the goal. In the calibration, the PA signal was measured by each transducer at all the locations along the circular path. Figure 12 illustrates the measured PA signals from 6 representative transducers over time-of-flight before and after the calibration. Before calibration, we see that the signal from the point target arrives each transducer at different time indicating positioning error (blue curves in Fig. 12). By adjusting the position of each transducer, we obtained the signals from the point target that arrived at the transducer at the same time point (red curves in Fig. 12). Figure 13 shows the reconstructed image of the three circular targets before and after the calibration. We see that the calibration provides much improved image reconstruction inters of the target shape and size.

1.4.2 Spatial Resolution

To evaluate the system spatial resolution, we constructed a phantom consisting of two point targets (brass wires; 100 μ m in diameter each) suspended in tissue phantom (solidified Intralipid scattering medium). Figure 14a shows the reconstructed image of the two point targets, while Figure 14b is the normalized profile of the reconstructed image along a line $y=10$ mm. From the profile, the half-width-at-half-maximum (AB) and the half-width-at-quarter-maximum (CD) were calculated to be 0.13mm. Using the resolution criterion, the spatial resolution of the system was estimated to be $AB+CD-target\ diameter=0.13+0.13-0.1=0.16\text{mm}$.

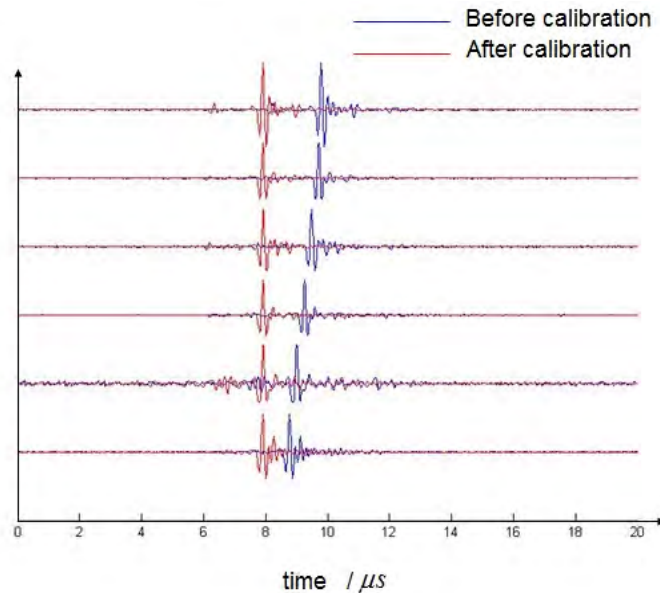


Figure 12. Measured PA signals from 6 representative transducers before and after the calibration.

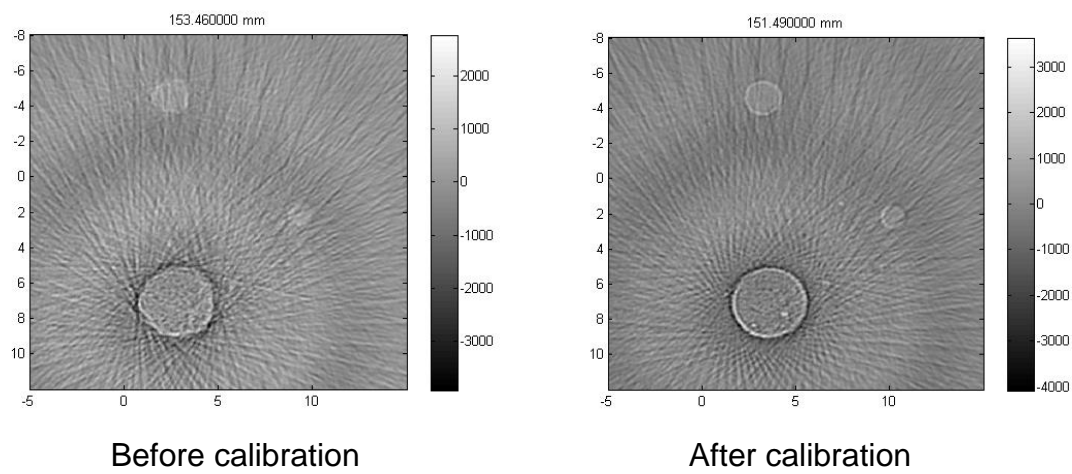


Figure 13 Reconstructed photoacoustic images of three circular targets before and after calibration.

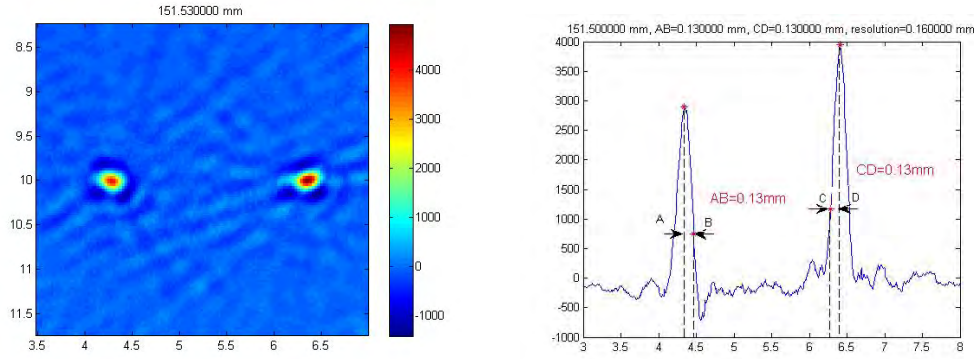


Figure 14 (a) Reconstructed image of two point targets. (B) The normalized profile of the reconstructed image shown in (A) along $y=10$ mm.

1.4.3 Phantom Evaluation

Phantom experiments that simulate detection of seizure focus have been conducted. Fig. 15a shows the recovered photoacoustic image of 0.1mm-diameter target mimicking a single seizure focus, while Fig. 15b gives the reconstructed image of three targets having a diameter of 4 mm, 1.2 mm and 0.6 mm, simulating multiple seizure foci. All the images obtained show that these targets with different sizes can be clearly detected using our imaging system.

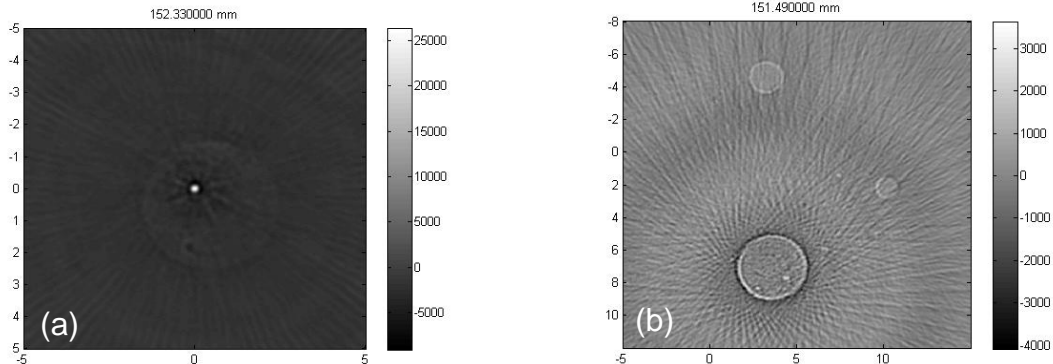


Figure 15 Reconstructed image of a single target (a) and three targets (b).

Figure 16 presents cross-sectional photoacoustic images of a simulated blood vasculature located at various depths ranging from 0 to 4.6 cm below the phantom surface. The cross-sections illustrate the capability of the system to provide high penetration imaging depth with high resolution and contrast at least at a depth up to 3.5 cm (Figures 16a and 16b show the photograph of the samples).

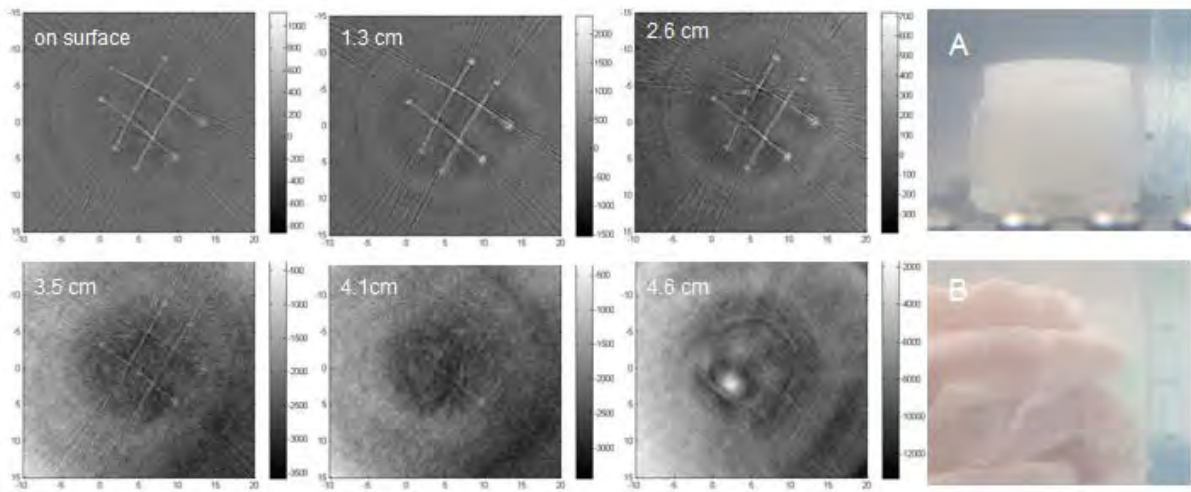


Figure 16 Cross-sectional images of simulated blood vasculature at various depths.

We also conducted phantom experiments to test the high temporal resolution ability of the system for real-time tomographic imaging of dynamic fluid flow (3-10Hz). Figure 17 depicts frames from a 10-second sequence of dynamic ink flow through a 1.6 mm-diameter polyethylene tube using a manual syringe push. To avoid partial view effects and maximize

temporal resolution, a sliding window acquisition was adopted in which element data from the nearest (or equal) time instant were used for image formation. The images obtained show that we can clearly track the flow through the tubing with high spatial and temporal resolution. Such tomographic imaging dynamic fluid flow was previously impossible. This will provide a powerful tool for *in vivo* real-time monitoring of brain hemodynamics during epileptic seizure onset.

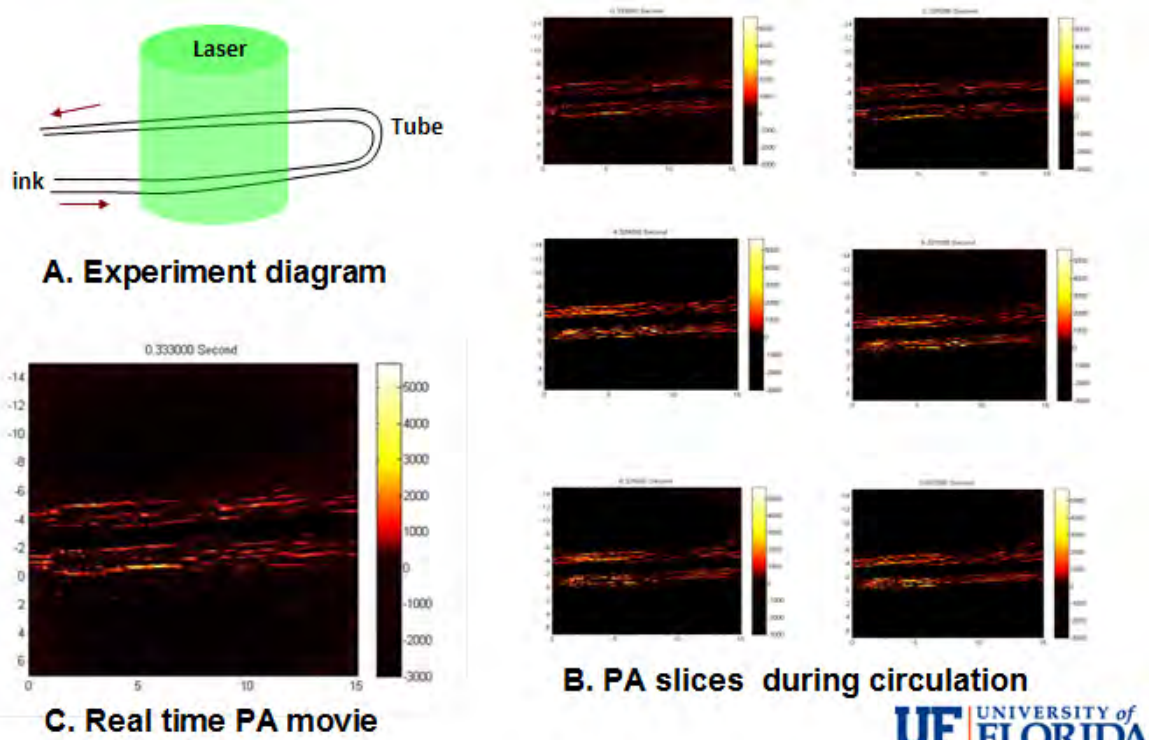


Figure 17 Photoacoustic images of dynamic ink flow through a 1.6 mm diameter tube.

1.4.4 Animal Interface and Initial *In Vivo* Testing of the System

We have constructed the animal interface, an animal chamber with adjustable vertical position with respect to the transducer array (see Fig. 18). During an experiment, the rat head is placed into the imaging region through an opening covered with a piece of polyethylene membrane at the top of the animal chamber.

We have performed initial animal/rat experiments to test the effectiveness of the animal interface for *in vivo* imaging. Figure 19a shows the cross-sectional photoacoustic image of a normal rat brain using the interface and the PAT system, while Figure 19b gives the open skull photograph of the same rat after the PAT imaging was performed. Compared to the open skull photograph, we see that major structures and various vasculature of the rat brain are clearly imaged with high quality. Figure 20 presents the recovered photoacoustic images of another rat brain at various depths ranging from 1 and 9 mm below the skin along with the open-skull photograph viewed from dorsal and basal surfaces. At the dorsal plane, the superior sagittal and cerebral veins including branches are visible in addition to the eyes. At the deeper cross-sections, the basilar veins and the middle cerebral artery can be observed along with ringed features near the brain stalk not visible in the photograph. This demonstrates that our photoacoustic imaging system has the potential to provide 3D imaging of the rat brain for accurate epileptic seizure localization.

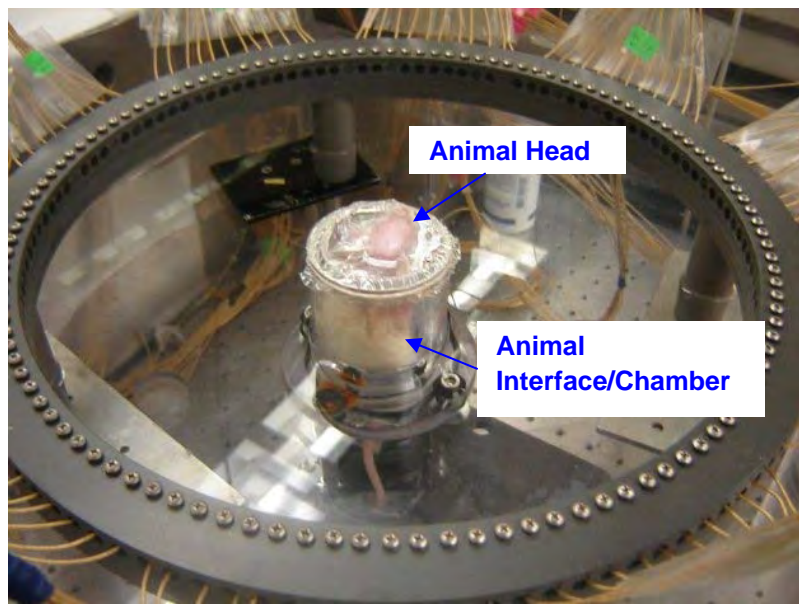
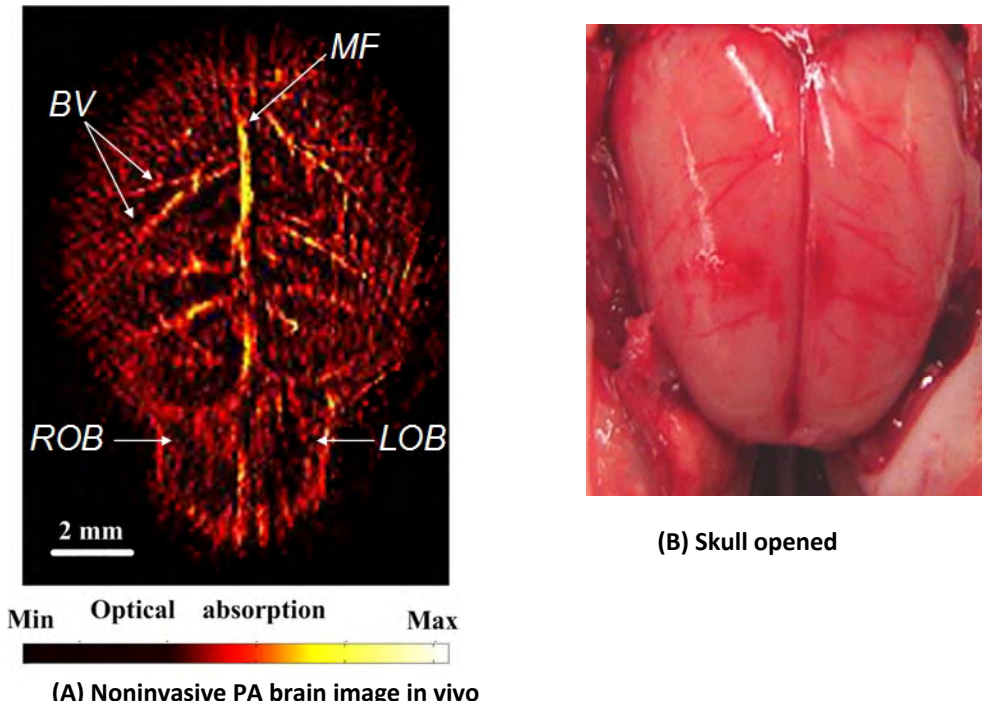
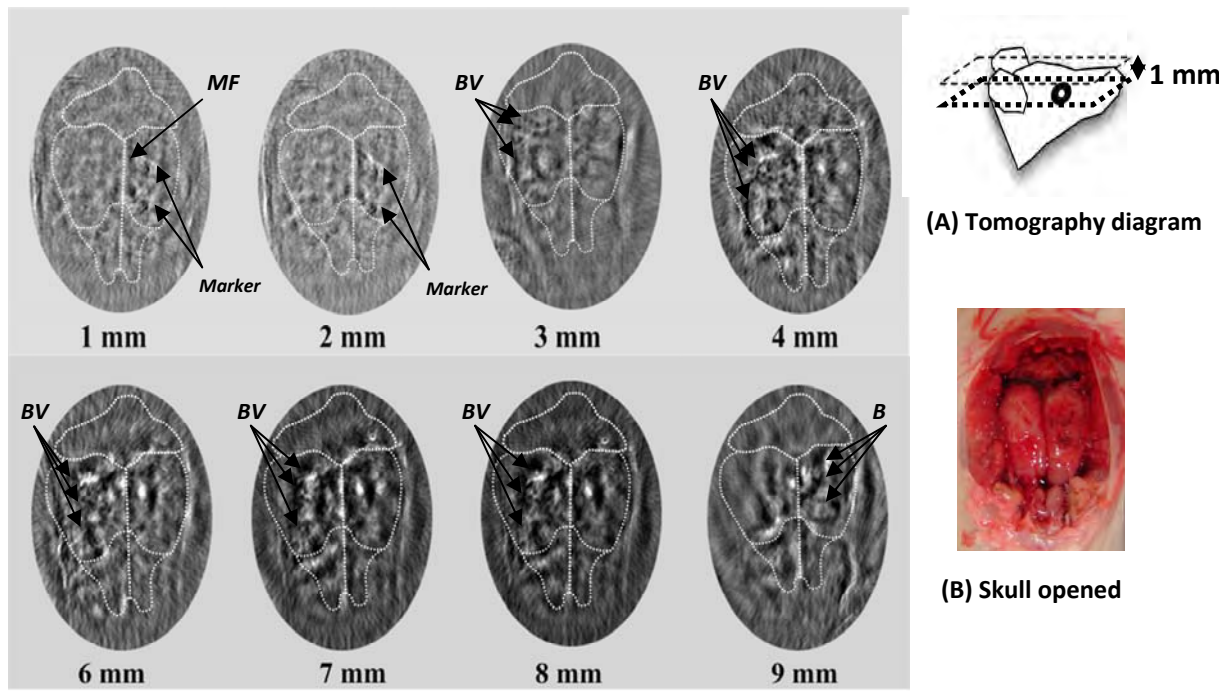


Figure 18 The photograph of the animal interface and transducer array.



(A) Noninvasive PA brain image *in vivo*

Figure 19 (a) Recovered photoacoustic image for a normal rat brain. The color scale (below) represents the optical absorption of tissue (arbitrary units). (b) Photograph of the rat cerebral with the skull opened.



(C) Cross-sectional images of rat brain vasculature at various depths

Figure 20 Recovered photoacoustic images of a normal rat brain at various depths below the skin.

2. Software Development (Tasks 3 and 4)

In Task 3, we proposed to implement 6 image enhancement schemes. In Year 1, 3 schemes including total variation (TV), advanced regularization techniques, and adaptive meshing were developed successfully. In Year 2, the remaining 3 schemes, including dynamic dual meshing, initial parameter optimization, and reconstruction of absolute optical absorption coefficient for quantitative high resolution functional PAT have been implemented as proposed.

2.1 Dynamic dual meshing

The concept of dual meshing is to decouple the spatial parameterization of the image property to be reconstructed from the model-based solution for the measured quantity. This allows specification or discretization of the reconstruction parameter to be independent of the model solution which is a powerful approach in that it lets the sampling density of these two quantities be distinct. Hence, the use of dual mesh method can considerably reduce computational costs during image formation while improving the accuracy of image reconstruction.

In Year 2, we have developed the proposed dynamic dual meshing scheme that is able to automatically solve the problem of mesh overlapping encountered for epilepsy imaging. In particular, the new scheme can achieve adaptive dual meshing that uses information about the resultant image as it evolves during the iterative reconstruction process. Consequently it has the capability to adapt the dual mesh node deployment into a more optimal spacing for the specific image under construction.

Two phantom experiments were conducted to test the dynamic dual meshing scheme. We employed single-target-containing phantom tests, aiming to validate the accuracy improvement

in detecting target when the dynamic dual mesh is used. The phantom materials used consisted of Intralipid as scatter and India ink as absorber with Agar powder (1-2%) for solidifying the Intralipid and India ink solution. The absorption coefficient of the background phantom was 0.01 mm^{-1} , while the absorption coefficient of the target was 0.015 mm^{-1} and 0.02 mm^{-1} for test 1 and test 2, respectively.

Figure 21 shows the evolution of finite element mesh during inverse iteration procedure when the new scheme is used for PAT. Figure 22 shows the reconstructed photoacoustic images for the two cases with uniform mesh and dynamic dual mesh. We see that the target is clearly better recovered with the dynamic dual mesh (a & d) in terms of its shape and size over that with the uniform mesh (c & f) for both cases. We also note that the background region for both cases is more smoothly recovered using the new scheme compared to that using the uniform mesh.

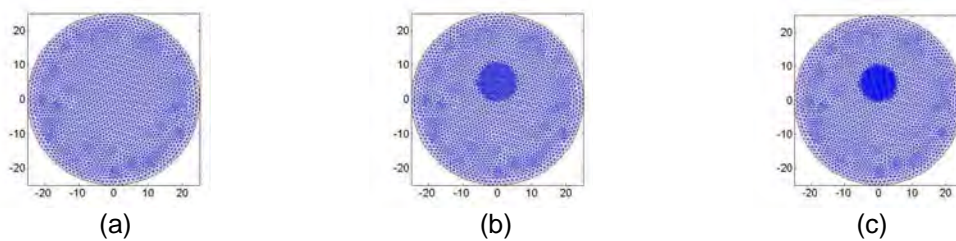


Fig. 21 (a) The initial mesh used for image reconstruction; (b) Dynamic adaptive mesh generated after the 1st iteration with one-time refinement; (c) Dynamic mesh generated after the 2nd iteration.

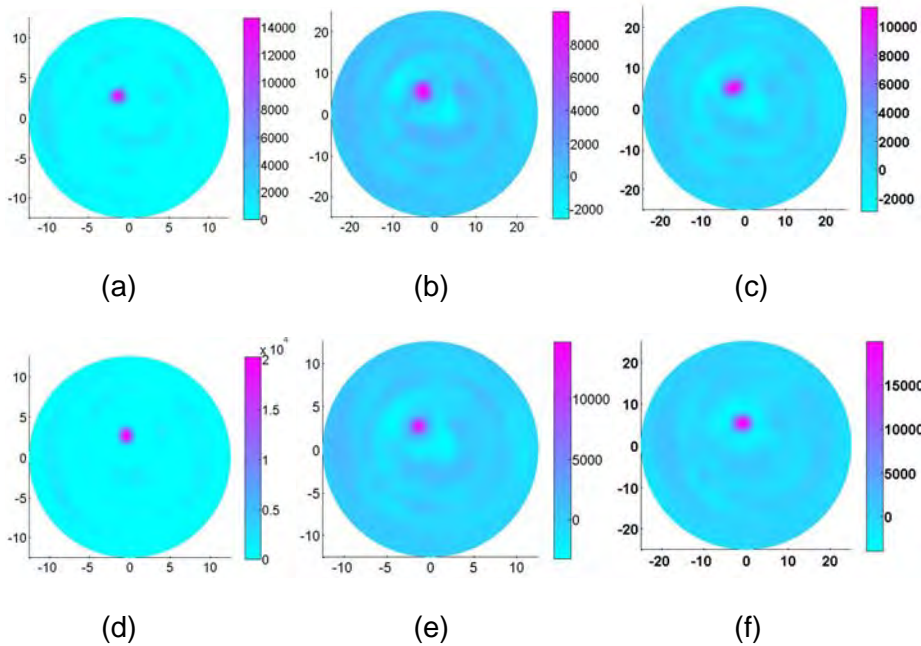


Fig. 22 Reconstructed photoacoustic images from experimental data. (a): the image for case 1 with dynamic dual mesh. (b): the image for case 1 with dynamic dual mesh after 1 iteration. (c): the image for case 1 with uniform mesh. (d): the image for case 2 with dynamic dual mesh. (e): the image for case 2 with dynamic dual mesh after 1 iteration. (c): the image for case 2 with uniform mesh.

2.2 initial parameter optimization

It has been shown in optical image reconstruction that we have realized a novel scheme to optimize the boundary conditions (BCs) coefficients as well as other initial parameters including the initial estimates of the optical properties. Based on this experience, in Year 2, we have implemented a new scheme to optimize the initial parameters needed for image reconstruction in PAT, which utilizes the parallel structure that is able to significantly reduce the computational costs for the data pre-processing.

Fig. 23 shows a set of typical reconstructions for the optimization of initial parameters study where the acoustic velocity is varied from 1.0×10^6 to 1.6×10^6 mm/s for a test case having one target embedded in a circular background medium. We note that the optimized initial parameters, particularly the acoustic velocity is useful in reducing the noise effect in the background and improve the quantitative nature of the recovered absorbed energy density.

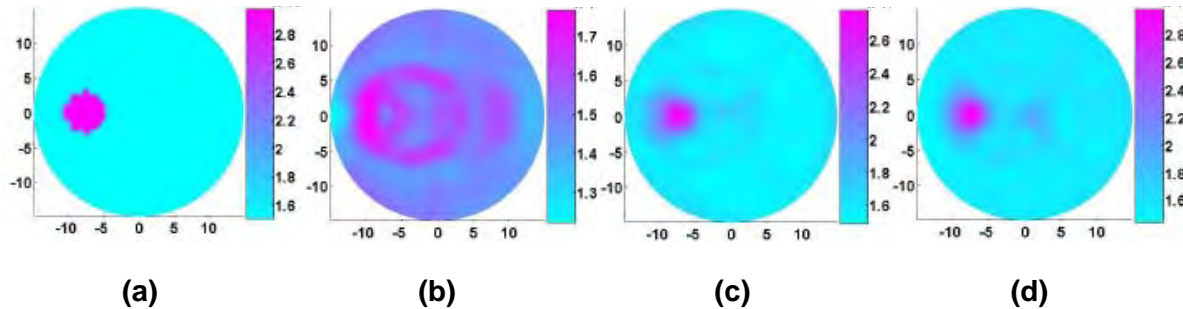


Fig. 23 (a): Exact distribution map of absorbed energy density. (b): Recovered energy density map with velocity equal to 1.0×10^6 (b), 1.4×10^6 (c), and 1.6×10^6 mm/s (d).

2.3 Reconstruction of absolute optical absorption coefficient for quantitative high resolution functional PAT

One major limitation of the existing method for reconstructing absorption coefficient is that it requires the measurement of the absolute excitation light strength. In addition, it does not use regularization techniques, thus the inverse solution procedure sometimes is not stable. To overcome these limitations, we have developed a novel reconstruction method, where images of optical absorption coefficient are obtained from a diffusion equation based regularized Newton method with the absorbed energy density distribution from conventional photoacoustic tomography serving as the measured field data. To recover the absorption coefficient from the absorbed energy density, Φ , the photon diffusion equation as well as the Robin boundary conditions(BCs) can be written in consideration of $\Phi = \mu_a \Psi$,

$$\nabla \cdot D(r) \nabla (E(r) \Phi(r)) - \Phi(r) = -S(r) \quad (1)$$

$$-D \nabla (E(r) \Phi) \cdot n = E(r) \alpha \Phi \quad (2)$$

where μ_a is the optical absorption coefficient, Ψ is the photon density, $E(r) = 1/\mu_a(r)$, $D(r)$ is the diffusion coefficient, $D = 1/(3(\mu_a + \mu'_s))$ and μ'_s is the reduced scattering coefficients, α is a boundary condition coefficient related to the internal reflection at the boundary, and $S(r)$ is the incident point or distributed source term. For the inverse computation, the initial estimate of inverse of absorption coefficient can be updated based on iterative Newton method as follows

$$\Delta(\mathbf{E}) = (\mathbf{J}^T \mathbf{J} + \lambda \mathbf{I} + \mathbf{L}^T \mathbf{L})^{-1} [\mathbf{J}^T (\Phi^o - \Phi^c)] \quad (3)$$

in which \mathbf{L} is the filter matrix, λ is the regularization parameter and \mathbf{J} is the Jacobian matrix. We experimentally demonstrate this new method using tissue-mimicking phantom measurements. For the two experiments, the phantom materials used consisted of Intralipid as scatterer and

India ink as absorber with Agar powder (1-2%) for solidifying the Intralipid and India ink solution. The background phantom had $\mu_a = 0.01 \text{ mm}^{-1}$ and $\mu_s = 1.0 \text{ mm}^{-1}$ while the two targets had $\mu_a = 0.03 \text{ mm}^{-1}$ and $\mu_s = 2.0 \text{ mm}^{-1}$ for test 1, and $\mu_a = 0.07 \text{ mm}^{-1}$ and $\mu_s = 3.0 \text{ mm}^{-1}$ for test 2. Figs. 24(a) and 24(b) present the reconstructed absorption coefficient images of two objects having a size of 2.0 and 3.0 mm (test 1), and 5.5 mm (test 2) in diameter, respectively, while the recovered absorbed energy density maps for experiments 1 and 2 are plotted in Figs. 24(c) and 24(d) for comparison. The reconstruction results show that the optical absorption coefficient images obtained are quantitative in terms of the shape, size, location and optical property values of the heterogeneities examined.

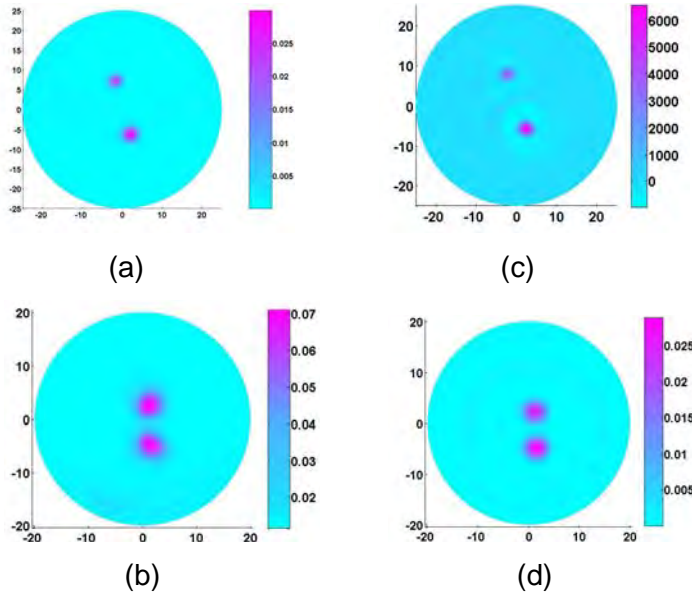


Fig. 24 Reconstructed absorption coefficient images (a, b) and absorbed optical energy density images (c, d) for tests 1 and 2. (a) and (c) are for test 1, and (b) and (d) for test 2.

Key Research Accomplishments

1. We have completed the construction of the proposed an array based real-time PAT system, and calibrated and tested the system using extensive phantom experiments.
2. We have built the animal interface and successfully tested it for *in vivo* imaging of rat brain.
3. We have developed three novel schemes that can enhance our current reconstruction software.
4. We have conducted phantom experiments that confirmed our software enhancement.

Reportable Outcomes (see the Appendix to this Summary Report)

We expect that the PAT system completed in Year 2 will allow us to generate considerable data for writing numerous journal publications and conference proceedings in Year 3.

Conclusions

We have made a significant progress that has fulfilled the statement of work proposed for Year 2 of this project. The real-time PAT system completed in Years 1 and 2 provides us a platform for performing the extensive phantom and animal experiments proposed for the coming years. We are confident that we will be able to fulfill or exceed the work statement for Years 3 and 4.

Appendix

L. Yao and H. Jiang, Enhancing finite element based photoacoustic tomography using total-variation minimization, *Physics in Medicine and Biology* (submitted).

Enhancing finite element based photoacoustic tomography using total-variation minimization

Lei Yao and Huabei Jiang*

Department of Biomedical Engineering
University of Florida
Gainesville, FL 32611

*Corresponding author

Tel: 352-273-9336 Fax: 352-273-9221 Email: hjiang@bme.ufl.edu

Submitted to *Phys. Med. Biol.*

Abstract

A total-variation-minimization-based finite element reconstruction algorithm for photoacoustic tomography is described in this paper that enhances the quality of reconstructed photoacoustic images with time-domain data. Simulations are conducted where different contrast levels between the target and the background, different noise levels, different sizes of and shapes of the target are studied in a 30mm-diameter circular heterogeneous background. These simulated results show that the quality of the reconstructed images can be improved significantly due to the decreased sensitivity to noise effect when the total-variation minimization is included. The enhancement is further confirmed using experimental data obtained from several phantom experiments and an *in vivo* animal experiment.

1. Introduction

Photoacoustic tomography (PAT) is an emerging non-invasive imaging technique that combines the merits of high optical contrast and high ultrasound resolution in a single modality [1-3]. In PAT, the Helmholtz-like photoacoustic (PA) wave equation has been commonly used as an accurate model for describing laser-induced acoustic wave propagation in tissue. While analytical reconstruction methods have been used for photoacoustic image reconstructions, the finite element method (FEM) based approach appears to be particularly powerful in this regard [4-5]. The advantages of the FEM based PAT method include (1) quantitative imaging capability by recovering optical absorption coefficient, (2) elimination of the assumption of homogeneous acoustic medium needed in analytical methods, (3) accommodation of object boundary irregularity, and (4) appropriate boundary conditions implementations.

Our finite element PAT approaches are based on a regularized iterative Newton method, which have been tested and evaluated using extensive simulations and phantom experiments in both frequency- and time-domain [4-7]. While these results are encouraging and promising, we realize that measurement noises are still the major factor affecting the quantitative accuracy of the reconstructed images. For example, errors for quantitatively recovering optical absorption coefficient can be as large as 10% for simulated data with 5% noise added and 20% for experimental data [6-7].

In an effort to reduce the noise effect and to further enhance the quantitative accuracy of photoacoustic image reconstruction, in this paper we consider a total-variation-minimization scheme within our FEM-based reconstruction framework. Our existing reconstruction algorithms are based on the least-squares criteria (i.e., the regularized

Newton method) [11-12] that stand on the statistical argument that the least-squares estimation is the best estimator over an entire ensemble of all possible pictures. Total variation, on the other hand, measures the oscillations of a given function and does not unduly punish discontinuities [8-9]. Hence, one can hypothesize that a hybrid of these two minimization schemes should be able to provide higher-quality image reconstructions. In fact, the strategy of finding minimal total-variation has proved to be successful in applications including electrical-impedance tomography [9], microwave imaging [10], image processing [8, 13-14], optimal design [15] and diffuse optical tomography [16].

In the following sections, we will describe in detail the implementation of total-variation-minimization within our existing PAT reconstruction framework in time-domain. We will demonstrate the enhanced reconstruction algorithm using simulated, phantom and in vivo data.

2. Total-Variation-Minimization Scheme

To describe our total-variation-minimization (TVM) method, we first briefly introduce the FEM-based regularized Newton method in time-domain [7]. The time-domain photoacoustic wave equation in tissue can be described as follows

$$\nabla^2 p(\mathbf{r}, t) - \frac{1}{v_0^2} \frac{\partial^2 p(\mathbf{r}, t)}{\partial t^2} = -\frac{\Phi(\mathbf{r})\beta}{C_p} \frac{\partial J(t)}{\partial t}, \quad (1)$$

where p is the pressure wave; v_0 is the speed of acoustic wave in the medium; β is the thermal expansion coefficient; C_p is the specific heat; Φ is the absorbed energy density; $J(t) = \delta(t - t_0)$ is assumed in our study.

The finite-element discretization of Eq. (1) can then be written as

$$\sum_{j=1}^N p_j \left[\int_S \nabla \psi_i \cdot \nabla \psi_j dS \right] + \sum_{j=1}^N \ddot{p}_j \left[\int_S \frac{1}{v_0^2} \psi_i \psi_j dS \right] - \oint_l \psi_i \nabla p \cdot \hat{n} dl = \int_S \frac{\beta \Phi}{C_p} \frac{\partial J}{\partial t} \psi_i dS. \quad (2)$$

where ψ_j is the basis function.

The first-order absorbing boundary conditions used are [17-20]:

$$\nabla p \cdot \hat{n} = -\frac{1}{v_0} \frac{\partial p}{\partial t} - \frac{p}{2r}. \quad (3)$$

where \hat{n} is the unit normal vector.

In both the forward and inverse calculations, the unknown coefficient, Φ needs to be expanded in a similar fashion to p as a sum of unknown parameters multiplied by a set of locally spatially varying Lagrange-polynomial basis functions. Thus the matrix form of Eq. (2) becomes,

$$[K]\{p\} + [C]\{\dot{p}\} + [M]\{\ddot{p}\} = \{B\}, \quad (4)$$

where the elements of matrix $[K]$, $[C]$ and $[M]$ are

$$K_{ij} = \int_S \nabla \psi_i \cdot \nabla \psi_j dS + \frac{1}{2r} \oint_l \psi_i \psi_j dl;$$

$$C_{ij} = \frac{1}{v_0} \oint_l \psi_i \psi_j dl;$$

$$M_{ij} = \frac{1}{v_0^2} \int_S \psi_i \psi_j dS;$$

and the column vectors $\{p\}$, $\{\dot{p}\}$, $\{\ddot{p}\}$ and $\{B\}$ are

$$B_i = \frac{\beta}{C_p} \int_S \psi_i \left(\sum_k \psi_k \Phi_k \right) dS \cdot \frac{\partial J}{\partial t};$$

$$\{p\} = \{p_1, p_2, \dots, p_N\}^T; \quad \{\dot{p}\} = \{\dot{p}_1, \dot{p}_2, \dots, \dot{p}_N\}^T; \quad \{\ddot{p}\} = \{\ddot{p}_1, \ddot{p}_2, \dots, \ddot{p}_N\}^T,$$

Here the Newmark's time-stepping scheme has been used for the discretization of time dimension [21-22], which is a commonly used implicit method for the second-order propagation equations such as Eq. (4).

To form an image from a presumably uniform initial guess of the absorbed energy density distribution we need a method of updating Φ from its starting value. This update is accomplished through the least-squares minimization of the following functional:

$$F(p, \Phi) = \sum_{j=1}^M (p_j^0 - p_j^c)^2, \quad (5)$$

where p_j^0 and p_j^c are observed and computed acoustic field data for $i = 1, 2, \dots, M$ boundary locations. Using the regularized Newton method, we obtained the following equation for updating Φ :

$$(\mathfrak{J}^T \mathfrak{J} + \lambda \mathbf{I}) \Delta \chi = \mathfrak{J}^T (p^0 - p^c), \quad (6)$$

where $p^0 = (p_1^0, p_2^0, \dots, p_M^0)^T$, $p^c = (p_1^c, p_2^c, \dots, p_M^c)^T$, $\Delta \chi$ is the update vector for the absorbed optical energy density, \mathfrak{J} is the Jacobian matrix formed by $\partial p / \partial \Phi$ at the boundary measurement sites; λ is the regularization parameter determined by combined Marquardt and Tikhonov regularization schemes, and \mathbf{I} is the identity matrix.

Two typical approaches exist for minimizing total variation: a constrained minimization through the solution of the nonlinear PA equation [8, 23] and an unconstrained minimization by addition of the total variation as a penalty term to the least squares functional [10, 13-14, 24]. Solutions obtained with these two methods are essentially the same; however, from a computational standpoint, unconstrained minimizations are much easier to implement and require much less modifications to the existing algorithm [13]. Thus in this study the unconstrained TVM is used.

We now incorporate the total variation of Φ as penalty term by defining a new functional [9-10, 13]:

$$\tilde{F}(p, \Phi) = F(p, \Phi) + L(\Phi). \quad (7)$$

Here

$$L(\Phi) = \int \sqrt{\omega_\Phi^2 |\nabla \Phi|^2 + \delta^2} dx dy, \quad (8)$$

is the penalty term, ω_Φ and δ are typically positive parameters that need to be determined numerically. The minimization of Eq. (7) proceeds in standard fashion by the differentiation of \tilde{F} with respect to each nodal parameter that constitutes the Φ distribution; simultaneously all these relations are set to zero. These steps lead to the following nonlinear system of equations

$$\frac{\partial \tilde{F}}{\partial \Phi_i} = - \sum_{j=1}^M (p_j^o - p_j^c) \frac{\partial p_j^c}{\partial \Phi_i} + V_i, \quad (i = 1, 2, \dots, N), \quad (9)$$

where

$$V_i = \frac{\partial L}{\partial \Phi_i} = \int \frac{\omega_\Phi^2 \left[\left(\sum_{k=1}^N \Phi_k \frac{\partial \psi_k}{\partial x} \right) \frac{\partial \psi_i}{\partial x} + \left(\sum_{k=1}^N \Phi_k \frac{\partial \psi_k}{\partial y} \right) \frac{\partial \psi_i}{\partial y} \right]}{\sqrt{\omega_\Phi^2 \left[\left(\sum_{k=1}^N \Phi_k \frac{\partial \psi_k}{\partial x} \right)^2 + \left(\sum_{k=1}^N \Phi_k \frac{\partial \psi_k}{\partial y} \right)^2 \right] + \delta^2}} dx dy$$

Similarly to Eq. (6), the following matrix equation for TVM constrained inversion can be obtained

$$(\mathfrak{I}^T \mathfrak{I} + R + \lambda I) \Delta \chi = \mathfrak{I}^T (p^0 - p^c) - V, \quad (10)$$

where

$$R = \begin{bmatrix} \frac{\partial V_1}{\partial \Phi_1} & \frac{\partial V_1}{\partial \Phi_2} & \dots & \frac{\partial V_1}{\partial \Phi_N} \\ \frac{\partial V_2}{\partial \Phi_1} & \frac{\partial V_2}{\partial \Phi_2} & \dots & \frac{\partial V_2}{\partial \Phi_N} \\ \vdots & \vdots & \ddots & \vdots \\ \frac{\partial V_N}{\partial \Phi_1} & \frac{\partial V_N}{\partial \Phi_2} & \dots & \frac{\partial V_N}{\partial \Phi_N} \end{bmatrix}$$

and $V = \{V_1, V_2, \dots, V_N\}^T$.

3. Results and Discussion

In this section the TVM enhanced reconstruction algorithm is tested and evaluated using both simulated and experimental data. For comparative purposes, reconstructions without the TVM enhancement are also presented.

3.1 Simulations

In these simulations, a dual meshing method, as detailed elsewhere [6], is used for fast yet accurate inverse computation. The fine mesh used for the forward calculation consisted of 3627 nodes and 7072 elements, while the coarse mesh used for the inverse calculation had 930 nodes and 1768 elements. All the images obtained from the method without the TVM are the results of three iterations, while those obtained from the TVM-enhanced method are the results of fifteen iterations. (We found that larger number of iteration changed the solutions only by less than 0.5%). For the simulations presented, $\omega_\Phi = 0.5$ and $\delta = 0.001$ for the first, second and third cases, and $\omega_\Phi = 1.0$ and $\delta = 0.001$ for the fourth case were used.

For the first simulation, the test geometry is a 30mm-diameter circular background containing an off-center 4-mm-diameter target region. The target had $\Phi = 1.0 \text{ mJ/mm}^3$,

while the background had $\Phi = 2.0 \text{ mJ/mm}^3$. In this case the image reconstruction was performed with 0%, 10% and 25% noise added to the “measured” data. Fig. 1 gives two sets of absorbed energy density images recovered using the reconstruction method without (Figs. 1a,c,e) and with the TVM enhancement (Figs. 1b,d,f) under the conditions of different noise levels. As can be seen, enhancement of the reconstruction by the incorporation of the TVM is obvious over the method without the TVM. To provide a more quantitative assessment of these images, Fig. 2 is included, in which the reconstructed absorbed energy density profiles are displayed along transects through the target for the images shown in Fig. 1. We find that the TVM enhanced method not only can improve the quality of the recovered images, but also can decrease the sensitivity of the method to noise effect.

The second simulation is intended to investigate how the target size affects the TVM enhancement. In this case, no noise was added to the “measured” data, and the diameter of the off-center target was 2 mm. Figs. 3a and 3b give two sets of absorbed energy density images recovered using the method without the TVM (Fig. 3a) and with the enhancement (Fig. 3b), while Figs. 3c and 3d present the quantitative profiles of the absorbed energy density along transects through the target for the images shown in Figs. 1a, 1b and Figs. 3a, 3b. Again, considerable improvement can be observed from the reconstructed results when the TVM is invoked compared with the method without the TVM. It is also interesting to note that the enhancement for this case is more striking than that for the first one where the background contained a larger target.

The third simulation aims to see how the contrast level of the absorbed energy density between the target and the background impacts the TVM enhancement. In this case, no

noise was added to the “measured” data, and the off-center target had a diameter of 4mm and $\Phi = 1.5 \text{ mJ/mm}^3$. Figs. 4a and 4b present two sets of absorbed energy density images recovered using the method without the TVM (Fig. 4a) and with the TVM enhancement (Fig. 4b), while Figs. 4c and 4d show the quantitative profiles of the absorbed energy density along transects through the target for the images shown in Figs. 1a, 1b and Figs. 4a, 4b. We can see that the images formed by incorporation of the TVM are clearly enhanced qualitatively in visual content relative to that obtained using the method without the TVM. We also note that lower the contrast level is, larger the enhancement is.

In the fourth simulation, three targets having different shapes (circular, elliptical and rectangular) were embedded in the background, and the absorbed energy density of these targets was 2.5 mJ/mm^3 , 1.5 mJ/mm^3 and 2.0 mJ/mm^3 , respectively. A noise level of 25% was added to the “measured” data in this case. Fig. 5 shows the exact and the recovered absorbed energy density images as well as the quantitative absorbed energy density property profiles along the transect that crosses these targets. Again, the improvement in image quality is apparent.

3.2 Phantom and In Vivo Experiments

In this section both phantom and in vivo experimental data were used to confirm our findings from the simulations. The experimental setup used for collecting the phantom data was a pulsed Nd: YAG laser based single transducer (1MHz) scanning system, which was described in detail elsewhere [5]. Three phantom experiments were conducted. In the first two experiments, we embedded one or two objects with a size ranging from 3 to 0.5 mm in a 50 mm-diameter solid cylindrical phantom. The phantom materials used consisted of Intralipid as scatterer and India ink as absorber with Agar

powder (1-2%) for solidifying the Intralip id and India ink solution. The absorption coefficient of the background phantom was 0.01 mm^{-1} , while the absorption coefficient of the target(s) was 0.03 mm^{-1} . In the last experiment, we used a single-target-containing phantom, aiming to test the capability of detecting target having low optical contrasts relative to the background phantom. In this case, the target had an absorption coefficient of 0.015 mm^{-1} . The reduced scattering coefficients of the background phantom and targets were 1.0 and 3.0 mm^{-1} for the first two experiments, and 1.0 and 2.0 mm^{-1} for the last experiment.

A total of 120 receivers were equally distributed along the surface of the circular background region. In the reconstructions, the fine mesh used for the forward calculation consisted of 5977 nodes and 11712 elements, while the coarse mesh used for the inverse calculation had 1525 nodes and 2928 elements. The reconstructed images were the results of three and fifteen iterations for the method without and with the TVM, respectively. For these experimental cases, $\omega_\phi = 1.0$ and $\delta = 0.001$ for the first and third cases and $\omega_\phi = 2.0$ and $\delta = 0.001$ for the second case were used.

Figure 6 shows the reconstructed absorption coefficient images for all the three experimental cases, while Figure 7 presents quantitative absorption coefficient profiles along transects through one target for the images shown in Fig. 6. We see that considerably enhanced images are achieved with the total-variation minimization, especially when the target is small (case 2), or when the contrast level between the target and the background is low (case 3).

As a final example, our methods were tested using in vivo data collected previously from an animal (rat) model of epilepsy [25]. Focal seizures were induced by

microinjection of bicuculline methiodide (BMI) into the parietal neocortex. The in vivo images were collected using the same pulsed ND: YAG laser based scanning PAT system. In the reconstruction, the fine mesh used for the forward calculation consisted of 17713 nodes and 34944 elements, while the coarse mesh used for the inverse calculation had 4489 nodes and 8736 elements. The in vivo images obtained were the results of two and five iterations for the methods without and with the TVM, respectively. We found that $\omega_\Phi = 0.1$ and $\delta = 0.001$ appeared to provide optimal results.

Fig. 8 gives the recovered images for the rat brain scanned 10 min after the injection of BMI without and with the use of the TVM. The in vivo results shown here confirm that both of the reconstruction methods can provide quality images (The arrow indicates the detected seizure focus), while no notable enhancement in image quality can be observed with the TVM based method. For example, the actual continuous middle cerebral artery (indicated by the dashed circle) is shown discontinued in Fig. 8a (without the TVM), while this feature is clearly depicted in Fig. 8b (with the TVM).

4. Conclusions

We have presented a time-domain FEM based photoacoustic image reconstruction method that incorporates the TVM. The results shown in this work indicate that the TVM based method is able to offer clear enhancement in image reconstruction over the method without the TVM, not only in terms of the location, size and shape of the target, but also the absorbed energy density property/optical absorption coefficient values themselves. In addition, the results have shown that the inclusion of the TVM in our reconstruction algorithm is highly effective in the presence of noisy data. Finally, it is important to note that the TVM based method may be ideal for image reconstruction involving a low

contrast level between the target and the background, or small targets embedded in the background.

Acknowledgement

This research was supported in part by the Department of Defense Congressionally Directed Medical Program.

References

- [1] G. Paltauf, J. Viator, S. Prahl, and S. Jacques, "Iterative reconstruction algorithm for optoacoustic imaging," *J. Acoust. Soc. Am.* **112**, 1536-1544 (2002).
- [2] S. J. Norton and T. Vo-Dinh, "Optoacoustic diffraction tomography: analysis of algorithms," *J. Opt. Soc. Am. A* **20**, 1859-1866 (2003).
- [3] A. A. Oraevsky, A. A. Karabutov, S. V. Solomatkin, E. V. Savateeva, V. A. Andreev, Z. Gatalica, H. Singh, R. D. Fleming, "Laser optoacoustic imaging of breast cancer in vivo," in *Biomedical Optoacoustics II*, ed A. A. Oraevsky, Proc. SPIE **4256**, 6-15 (2001).
- [4] Z. Yuan and H. Jiang, "Quantitative photoacoustic tomography: Recovery of optical absorption coefficient maps of heterogenous media," *Appl. Phys. Lett.* **88**, 231101 (2006).
- [5] L. Yin, Q. Wang, Q. Zhang, and H. Jiang, "Tomographic imaging of absolute optical absorption coefficient in turbid media using combined photoacoustic and diffusing light measurements," *Opt. Lett.* **32**, 2556-2558 (2007).

[6] H. Jiang, Z. Yuan, and X. Gu, “Spatially varying optical and acoustic property reconstruction using finite-element-based photoacoustic tomography,” *J. Opt. Soc. Am. A* **23**, 878-888 (2006).

[7] L. Yao and H. Jiang, “Finite-element-based photoacoustic tomography in time-domain”, *J. Opt. A: Pure Appl. Opt.* **11**, 085301 (2009).

[8] D. C. Dobson and F. Santosa, “An image-enhancement technique for electrical impedance tomography,” *Inverse Probl.* **10**, 317-334 (1994).

[9] P. M. van den Berg and R. E. Kleinmann, “A total variation enhanced modified gradient algorithm for profile reconstruction,” *Inverse Probl.* **11**, L5-L10 (1995).

[10] C. R. Vogel and M. E. Oman, “Iterative methods for total variation denoising,” *SIAM J. Sci. Comput.* **17**, 227-238 (1996).

[11] K. D. Paulsen and H. Jiang, “Spatially-varying optical property reconstruction using finite element diffusion equation approximation,” *Med. Phys.*, **22**, 691-702 (1995).

[12] S. R. Arridge, “Forward and inverse problems in time-resolved infrared imaging,” in *Medical Optical Tomography: Functional Imaging and Monitoring*, G. J. Mueller, B. Chance, R. R. Alfano, S. B. Arridge, J. Beuthen, E. Gratton, M. Kaschke, b. R. Masters, S. Svanberg, and P. van der Zee, eds., Vol. IS11 of the SPIE institute Series (SPIE Press, Bellingham, Wash., 1993), 35-64

[13] D. C. Dobson and F. Santosa, “Recovery of blocky images from noisy and blurred data,” *SIAM J. Appl. Math.* **56**, 1181-1198 (1996).

[14] D. C. Dobson, “Exploiting ill-posedness in the design of diffractive optical structures,” in *Smart Structures and Materials 1993: Mathematics in Smart Structures*, H. Banks, eds., Proc. SPIE 1919, 248-257 (1993).

[15] R. Acar and C. R. Vogel, “Analysis of bounded variation penalty methods for ill-posed problems,” *Inverse Probl.* 10, 1217-1229 (1994).

[16] K. D. Paulsen and H. Jiang, “Enhanced frequency-domain optical image reconstruction in tissues through total-variation minimization”, *App. Opt.*, 35, 3447-3458 (1996).

[17] A. Bayliss and E. Turkel , “Radiation Boundary Conditions for Wave-Like Equations,” *Comm. Pure. Appl. Math.* 33, 707-725 (1980).

[18] R. Mittra and O. Ramahi, “Absorbing boundary conditions for the direct solution of partial differential equations arising in electromagnetic scattering problems,” in *Differential Methods in Electromagnetic Scattering*, ed J. A. Kong and M. A. Morgan, Elsevier, 133-173 (1989).

[19] H. Gan, P. L. Levin and R. Ludwig , “Finite element formulation of acoustic scattering phenomena with absorbing boundary condition in the frequency domain,” *J. Acoust. Soc. Am.* 94, 1651-1662 (1993).

[20] T. Van and A. Wood, “A time-domain finite element method for Helmholtz Equations,” *J. Comput. Phys.* 183, 486-507 (2002).

[21] I. M. Smith, D. V. Griffiths, *Programming the finite element method*, ed John Wiley & Sons, Chichester, UK (2004).

[22] O. C. Zienkiewicz, R. L. Taylor and J. Z. Zhu, *Finite element method: its basis and fundamentals*, Butterworth, Heinemann (2005).

[23] L. I. Rudin, S. Osher, and E. Fatemi, “Nonlinear total variation based noise removal algorithm,” *Physica D* **60**, 259-268 (1992).

[24] S. R. Arridge, P. van der Zee, M. Cope, and D. Delpy, “Reconstruction methods for infrared absorption imaging,” in *Time-Resolved Spectroscopy and Imaging of Tissues*, B. Chance and A. Katzir, eds., Proc. SPIE 1431, 204-215 (1991).

[25] Q. Zhang, Z. Liu, P. R. Carney, Z. Yuan, H. Chen, S. N. Roper and H. Jiang, “Non-invasive imaging of epileptic seizures *in vivo* using photoacoustic tomography,” *Phys. Med. Biol.* **53**, 1921-1931 (2008).

Figure captions

Fig.1 Reconstructed absorbed energy density images from simulated data with and without the total-variation-minimization (TVM) enhancement under different noise levels (case 1). (a), without the TVM, 0% noise. (b), with the TVM, 0% noise. (c), without the TVM, 10% noise. (d), with the TVM, 10% noise. (e), without the TVM, 25% noise. (f), with the TVM, 25% noise.

Fig.2 Comparison of the exact and reconstructed absorbed energy density profiles along transect $y=0\text{mm}$ for the images appearing in Fig.1. (a), 0% noise. (b), 10% noise. (c), 25% noise.

Fig.3 Reconstructed absorbed energy density images from simulated data with and without the total-variation-minimization (TVM) enhancement with different target sizes (case 2). (a), without the TVM, 2mm -diameter target. (b), with the TVM, 2mm -diameter target. (c), the absorbed energy density profiles along the transect $y=0\text{mm}$ for the images appearing in Figs. 1a and 1b (4mm -diameter target). (d), the absorbed energy density property profiles along the transect $y=0\text{mm}$ for the images appearing in Figs. 3a and 3b (2mm-diameter target).

Fig.4 Reconstructed absorbed energy density images from simulated data with and without the total-variation-minimization (TVM) enhancement with different contrast levels between the target and the background (case 3). (a), without the TVM, 1.5:1

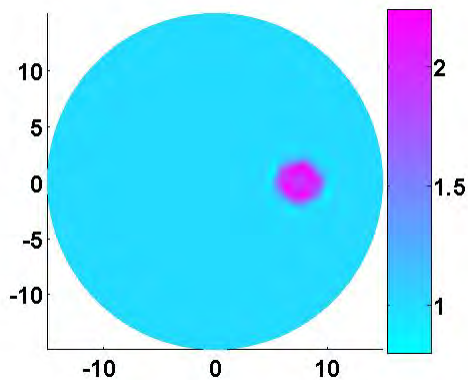
contrast. (b), with the TVM, 1.5:1 contrast . (c), absorbed energy density profiles along the transect $y=0\text{mm}$ for the im ages appearing in Figs. 1a and 1b (2:1 contrast). (d), absorbed energy density profile s along the transect $y=0\text{mm}$ for the im ages appearing in Figs. 4a and 4b (1.5:1 contrast).

Fig.5 Reconstructed absorbed energy density images from simulated data with and without the total-variation- minimization (TVM) enhancement for three targets having different shapes (case 4). (a), exact image. (b), without the TVM. (c), with the TVM . (d), the absorbed energy density profiles along the transect $y=0\text{mm}$.

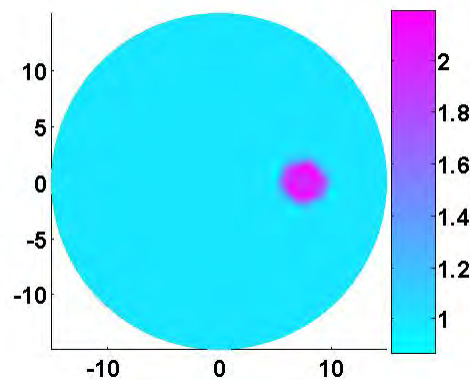
Fig.6 Reconstructed absorbed energy de nsity images from the three phantom experiments. (a), case 1 w ithout the TVM. (b), case 2 without the TVM, (c), case 3 without the TVM. (d), case 1 with the TVM. (e), case 2 with the TVM. (f), case 3 with the TVM.

Fig. 7 Recovered absorbed energy density profiles along (a) $y=-7.0\text{mm}$ crossing the 3mm-diameter target for experim ental case 1, (b) $y=8.0\text{mm}$ crossing the 2mm-diameter target for experimental case 1, (c) $y=1.0\text{mm}$ for experimental case 2, and (d) $y=6.5\text{mm}$ for experimental case 3.

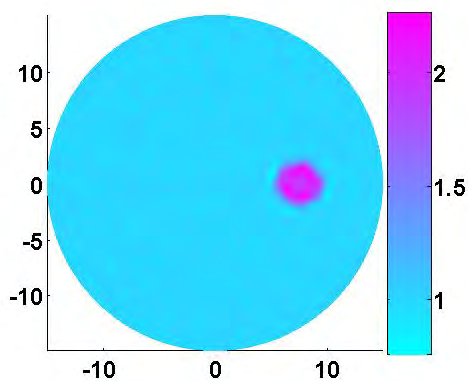
Fig. 8 Recovered absorbed energy density im ages from the rat brain. (a), without the TVM. (b), with the TVM.



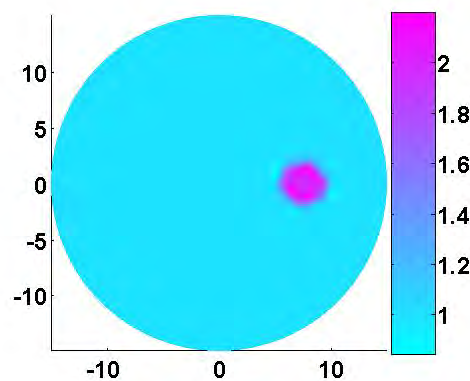
(a)



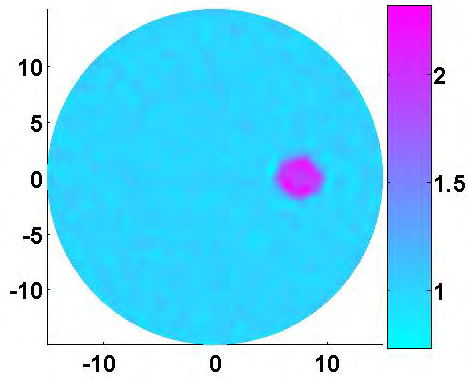
(b)



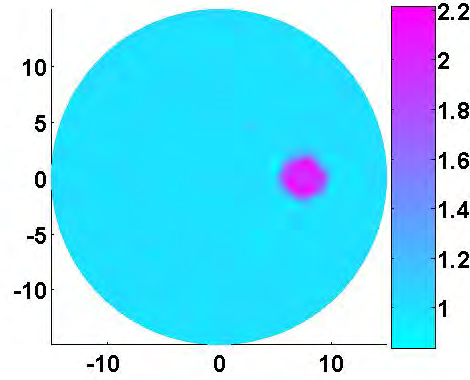
(c)



(d)



(e)



(f)

Fig. 1

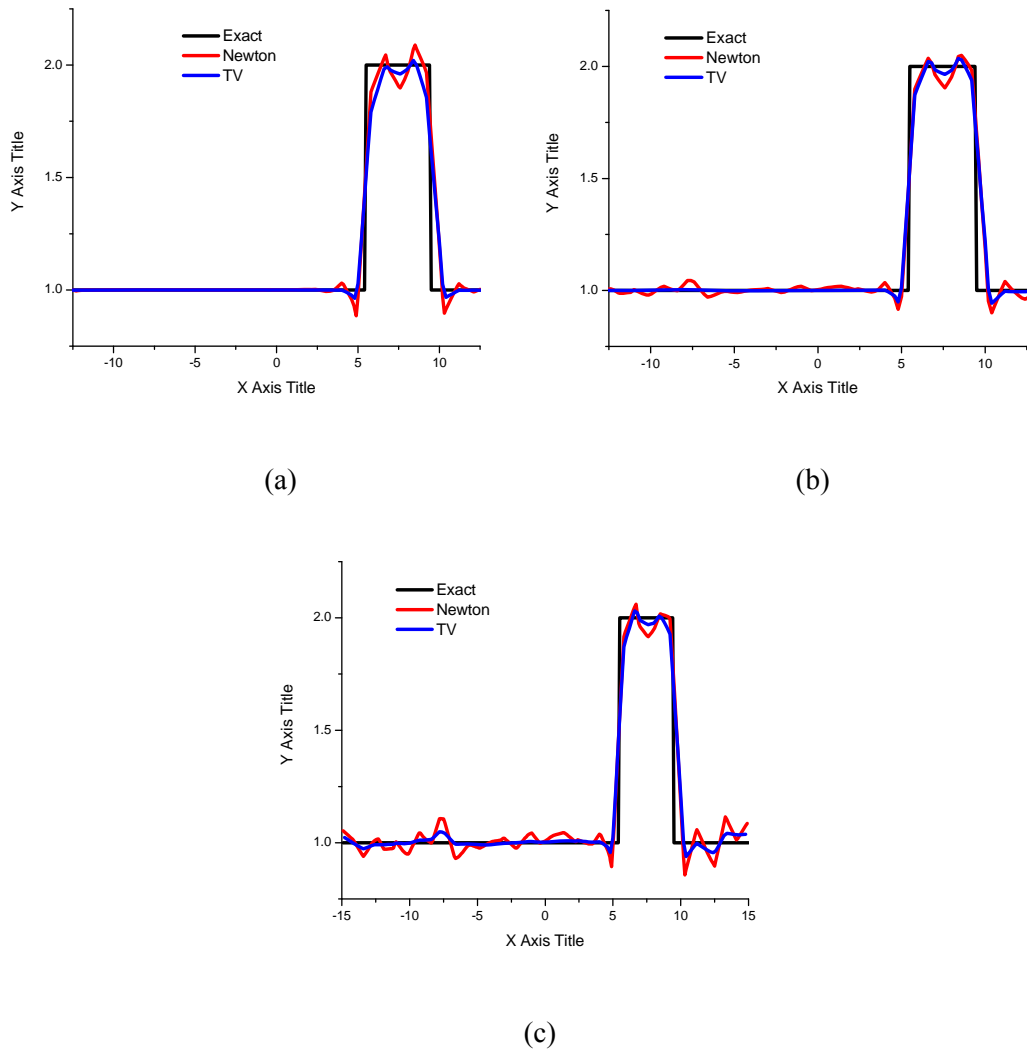
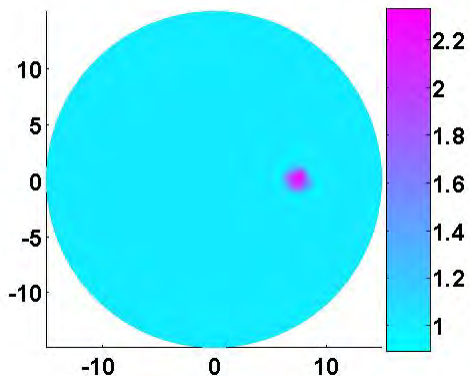
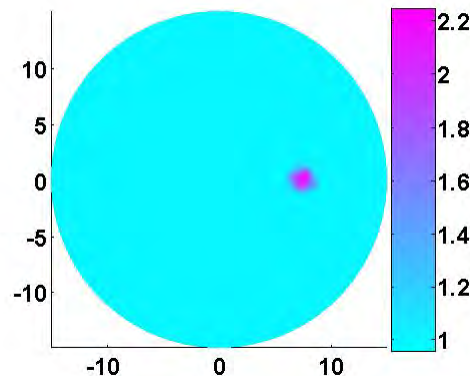


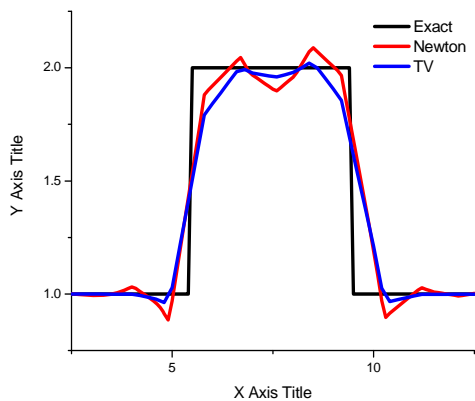
Fig. 2



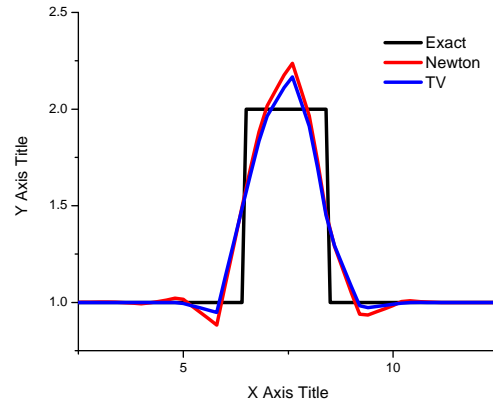
(a)



(b)

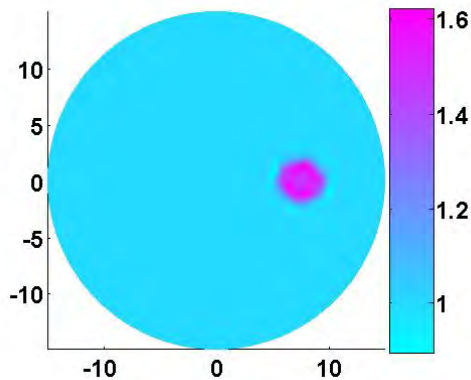


(c)

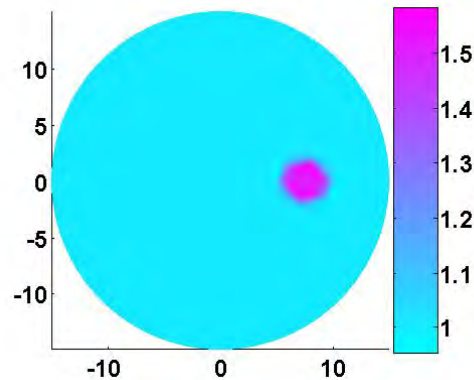


(d)

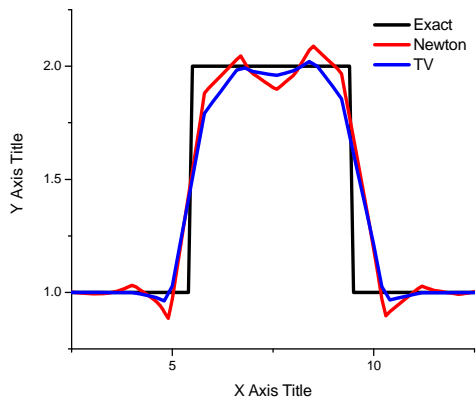
Fig.3



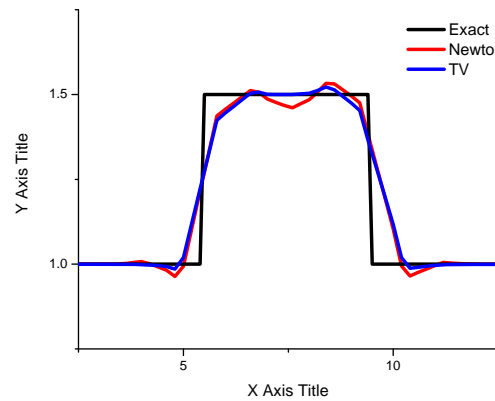
(a)



(b)

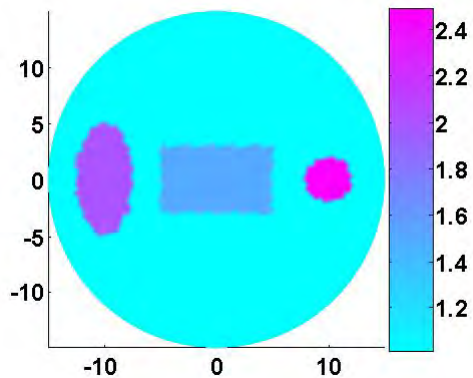


(c)

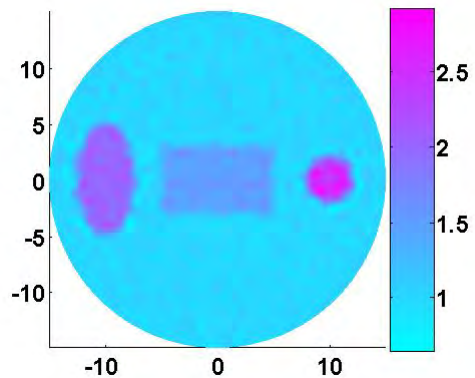


(d)

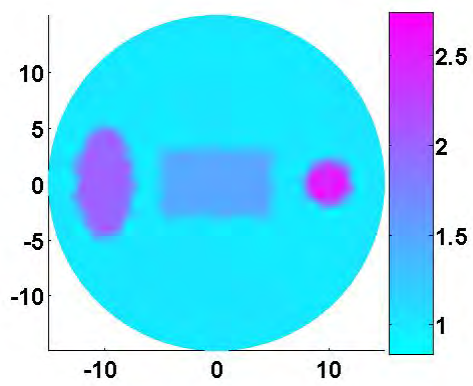
Fig.4



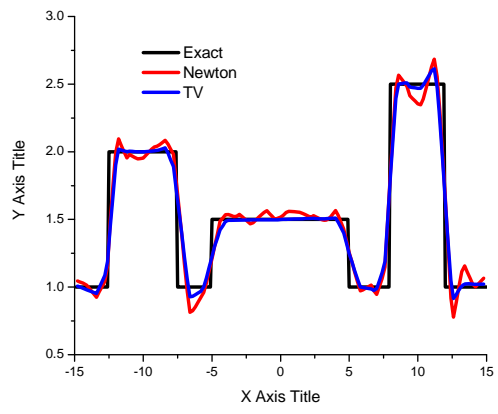
(a)



(b)

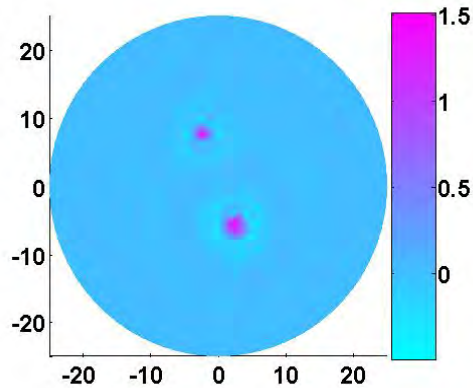


(c)

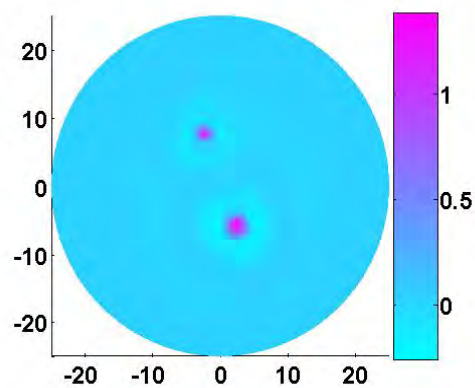


(d)

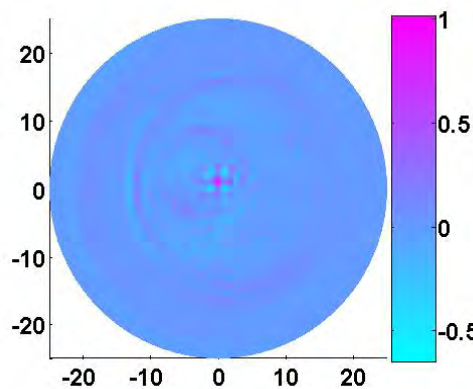
Fig. 5



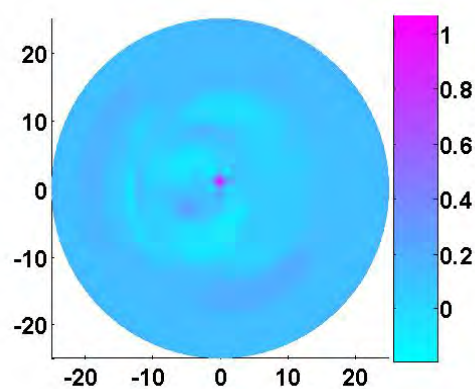
(a)



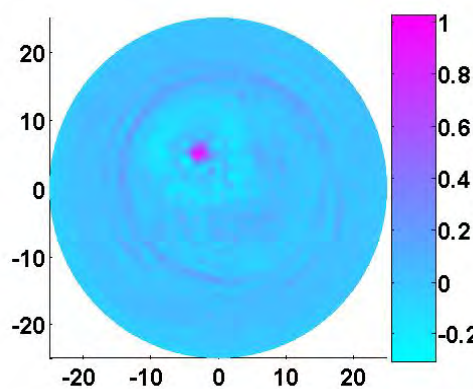
(b)



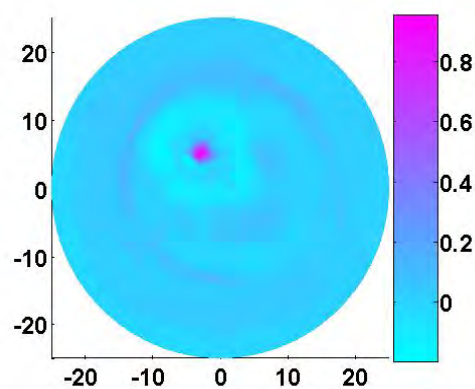
(c)



(d)



(e)



(f)

Fig. 6

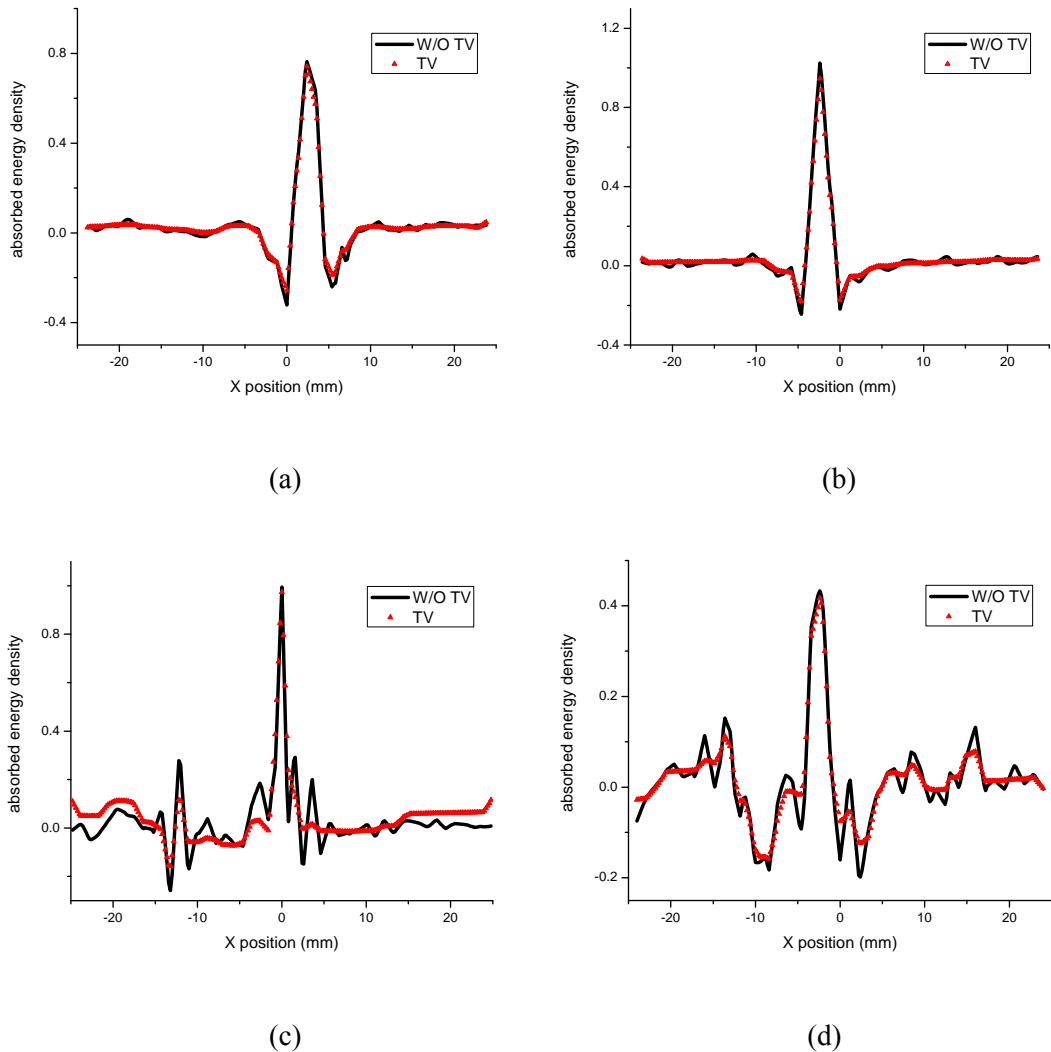
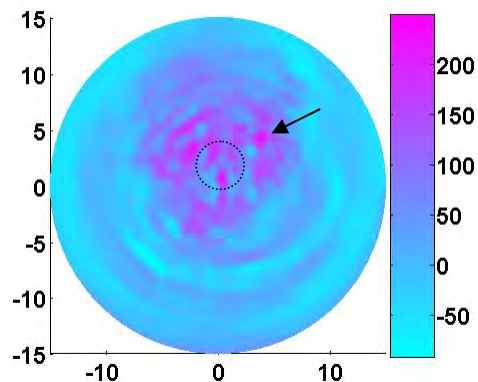
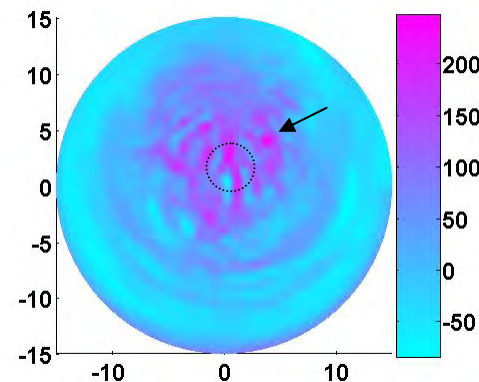


Fig. 7



(a)



(b)

Fig. 8